Strength and limits of transient mid to late Holocene simulations with dynamical vegetation

Pascale Braconnot*, Dan Zhu, Olivier Marti and Jérôme Servonnat

IPSL/Laboratoire des Sciences du Climat et de l'Environnement, unité mixte CEA-CNRS-UVSQ, Université Paris Saclay, Bât. 714, Orme de Merisiers, 91191 Gif-sur-Yvette Cedex.

Correspondance to : pascale.braconnot@lsce.ipsl.fr

Abstract. We present the first simulation of the last 6000 years with a version of the IPSL Earth System model that includes interactive dynamical vegetation and carbon cycle. It is discussed at the light of a set of mid Holocene and pre industrial simulations performed to set up the model version and to initialize the dynamical vegetation. These sensitivity experiments remind us that model quality or realism is not only a function of model parameterizations and tuning, but also of experimental set up. The transient simulations shows that the long term trends in temperature and precipitation have similar shape to the insolation forcing, except at the equator, in high latitudes and south of 40°S. In these regions cloud cover, sea-ice, snow, or ocean heat content feedbacks lead to smaller or opposite temperature responses. The long term trend in tree line in northern hemisphere is reproduced and starts earlier than the southward shift vegetation over the Sahel. Despite little change in forest cover over Eurasia, a long term change in forest composition is simulated, including large centennial variability. The rapid increase of atmospheric CO_2 in the last centuries of the simulation contributes to enhance tree growth and counteracts the long term trends induced by Holocene insolation in the northern hemisphere and amplify it in the southern hemisphere. We also highlight some limits in the evaluation of such a simulation resulting from model climate-vegetation biases, the difficulty to fully assess the result for pre-industrial or modern conditions that are affected by land-use, and the possibility for multi-vegetation state under modern conditions.

1 Introduction

Past environmental records such as lake levels or pollen records highlight substantial changes in the global vegetation cover during the Holocene (COHMAP-Members, 1988; Wanner et al., 2008). The early to mid-Holocene optimum period was characterized by a northward extension of boreal forest over north Eurasia and America which attests for increased temperature in mid to high latitudes (Prentice and Webb, 1998). A massive expansion of moisture and precipitation in Afro-Asian regions has been related to enhance boreal summer monsoon (Jolly et al., 1998; Lezine et al., 2011). These changes were triggered by latitudinal and seasonal changes in top of the atmosphere (TOA) incoming solar radiation caused by the long term variation in Earth's orbital parameters (Berger, 1978). During the course of the Holocene these features retreated towards their modern distribution (Wanner et al., 2008). While global data syntheses exist for the mid-Holocene (Bartlein et al., 2011; Harrison, 2017; Prentice et al., 2011), reconstructions focus in general on a location or a region when considering the whole Holocene. For example regional syntheses for long term paleo records over Europe reveal long term vegetation changes that can be attributed to changes in temperature or precipitation induced by insolation changes (Davis et al., 2003; Mauri et al., 2015). Similarly, over West Africa or Arabia, pollen data

suggests a southward retreat of the intertropical convergence zone (Lezine et al., 2017), and a reduction in North African monsoon intensity (Hély and Lézine, 2014). The pace of these changes varies from one region to the other (e.g. Fig. 6.9 in Jansen et al., 2007; Renssen et al., 2012) and has been punctuated by millennium scale variability or abrupt events (deMenocal et al., 2000), for which it is still unclear that they represent global or more regional events. How vegetation changes have been triggered by this long term climate change and what has been the vegetation feedback on climate is still a matter of debate.

Pioneer simulations with asynchronous climate-vegetation coupling suggested that vegetation had a strong role in amplifying the African monsoon (Braconnot et al., 1999; Claussen and Gayler, 1997; de Noblet-Ducoudre et al., 2000; Texier et al., 1997). When dynamical vegetation model were included in fully coupled ocean-atmosphere-sea-ice models, climate simulations suggested a lower magnitude of the vegetation feedback (Braconnot et al., 2007a; Braconnot et al., 2007b; Claussen, 2009). Individual model results indicates however that vegetation plays a role in triggering the African monsoon during mid-Holocene (Braconnot and Kageyama, 2015), but also that soil moisture might play a larger role than anticipated (Levis et al., 2004). Reduced dust emission with increased vegetation and changed soil properties have been shown to amplify monsoon changes (Albani et al., 2015; Egerer et al., 2017; Pausata et al., 2016). In high latitude as well, the role of the vegetation feedback is not fully understood. Previous studies showed that the response of vegetation in spring combined to the response of the ocean in autumn were key factors to transform the seasonally varying insolation forcing into an annual mean warming (Wohlfahrt et al., 2004). The magnitude of this feedback has been questioned by Otto et al. (Otto et al., 2009), showing that vegetation was mainly responding to the ocean and sea-ice induced warming over land. The role and magnitude of the vegetation feedback were also questioned over Asia (Dallmeyer et al., 2010). The variety of response of dynamical vegetation models to external forcing is an issue in these discussions. However they all produce increased vegetation in Sahel when forced with mid-Holocene boundary conditions, which suggests that, despite large uncertainties, robust basic response can be inferred from current models (Hopcroft et al., 2017). Other studies have highlighted that there might exist several possible vegetation distribution at the regional scale for a given climate that can be related to instable vegetation states (e.g. Claussen, 2009). This is still part of the important questions to solve to fully explain the end of the African humid period around 4000-5000 years BP (Liu et al., 2007).

It is not clear yet that more comprehensive models and long Holocene simulations can help solve all the questions, given all the uncertainties described above. But they can help to solve the question of vegetation-climate state and of the linkages between insolation, trace gases, climate and vegetation changes at global and regional scales. For this, we investigate the last 6000 years long term trend and variability of vegetation characteristics as simulated by a version of the IPSL model with an interactive carbon cycle and dynamical vegetation. Off line simulations, using the original scheme for dynamical vegetation of ORCHIDEE, were already used to analyze Mid-Holocene and LGM vegetation (Kageyama et al., 2013b; Woillez et al., 2011). This has not yet been done in the fully coupled system for long transient simulations. Previous studies clearly highlight that small differences in the albedo or soil formulation can have large impact on the simulated results (Bonfils et al., 2001; Otto et al., 2011). Given all the interactions in a climate system, the climatology produced by a model version with interactive vegetation is by construction different from the one of the same model with prescribed vegetation. In particular model biases are in general larger (Braconnot and Kageyama, 2015; Braconnot et al., 2007b), so that the corresponding simulations need to be considered as resulting from different

models (Kageyama et al., 2018). The way the external forcing is applied to the model can also lead to climatology or vegetation differences between two simulations with the same model. It is thus important to know how the changes we made to the IPSL climate model to set up the version with dynamical vegetation affect the results and the realisms we can expect from the transient simulations. We thus investigate first how the major changes and tuning affect the mid-Holocene simulations and the performances of the model compared to simulations with the previous model version IPSLCM5A (Dufresne et al., 2013; Kageyama et al., 2013a). Several questions guide the analyses of the transient experiment. Is the long term response of climate and vegetation a direct response to the insolation forcing? How large is the impact of the trace gases? How different is the timing of the vegetation in different regions? Do we need to care about variability over such a long time period? We also need to put the responses to these questions in perspective with the level of realism we can expect from the simulated vegetation in such a simulation. It concerns the model biases, the compatibility between the climate and vegetation states produced by the transient simulation or obtained from snap shot experiments. Also different strategies can be used to initialize the vegetation dynamics and produce the mid-Holocene initial state for the transient simulation. We investigate if they have an impact on the simulated vegetation distribution.

The remainder of the manuscript is organized as follow. Section 2 describes the experimental set up, the characteristics of the land surface model as well as different model adjustments we made, and the initial state for the dynamical vegetation. Section 3 presents the transient simulation focusing on long term climate and vegetation trends at global and regional scales. Section 4 discusses the realism of the simulated vegetation and different sources of uncertainties that can affect it, before the conclusion presented in section 5.

2 Model and the suite of experiments

2.1 Experimental design

The mid-Holocene (MH) time-slice climate experiment (6000 years BP) represents the initial state for the last 6000 years transient simulation with dynamical vegetation. It is thus considered as a reference climate in this study. Because of this, and to save computing time, model adjustments made to set up the model content and the model configuration were mainly done running MH and not pre-industrial (PI) simulations (Table 1 and 2). Only a subset of PI simulation is available for comparison with modern conditions. All the simulations were run long enough (300-1000 years) to reach a radiative equilibrium and be representative of a stabilized MH climate (Fig. 1). They are free of any artificial long term trends after the adjustment phase, as were IPSL PMIP3 MH simulations (Fig. 1, Kageyama et al., 2013a).

Most tests follow the MH PMIP3 protocol (Braconnot et al., 2012). This is only due to the fact that this work began before the PMIP4 boundary conditions were available. But the transient simulation (TRHOLV, for TRansient HOLocene simulation with dynamical Vegetation), and the 1000 year-long MH simulations with or without dynamical vegetation that were run to prepare the initial state for it, follows the PMIP4-CMIP6 protocol (Otto-Bliesner et al., 2017, Tab. 1). In all simulations the Earth's orbital parameters are derived from Berger (1978). The MH PMIP3 protocol uses the trace gases (CO_2, CH_4 and N_2O) reconstruction from ice core data by Joos and Spahni (2008). It has been updated for PMIP4, using new data and a revised chronology that provides a consistent history of the evolution of these gases across the Holocene (Otto-Bliesner et al., 2017). The

difference in forcing between PMIP4 and PMIP3 was estimated to be -0.8 $W.m^{-2}$ by Otto-Bliesner et al. (2017). This is the order of magnitude found for the imbalance in net surface heat flux at the beginning of the MH-FPMIP4 simulation. This simulation started from L11Aer run with PMIP3 protocol (Fig. 1a). It uses the same model version, but follows the PMIP4 protocol. For the subset of PI experiments Earth's orbit and trace gases are prescribed to year 1860, i.e. the beginning of the industrial area. For the MH and PI time slice experiments, boundary conditions do not vary with time. For the transient simulations the Earth's orbital parameters and trace gases are updated every year.

In standard versions of the IPSL model, aerosols are accounted for by prescribing the optical distribution of dust, sea-salt, sulfate and particulate organic matter (POM), so as to take into account the coupling between aerosols and radiation (Dufresne et al., 2013). For MH simulations these variables are prescribed to 1860 CE values, for which the level or sulfate and POM is slightly higher than the values found in the Holocene (Kageyama et al., 2013a). Here, except for the first few tests (Tab. 1), we prescribe only dust and sea-salt to their 1860 values and neglect the other aerosols. A fully coupled dust-sea salt-climate version of the model that does not consider the other aerosols is under development for long transient simulations. For future comparisons it is important to have similar model set up. Indeed, compared to the version with all aerosols, considering only dust and sea salts imposes a radiative difference of about 2.5 $W.m^{-2}$ in external climate forcing. Its footprint appears on the net heat flux imbalance at the beginning of L11Aer. It leads to a global air temperature increase of 1.5 °C (Fig. 1c). The largest warming over land is found in the northern hemisphere, but the ocean warms almost everywhere by about 1°C, except in the Antarctic circumpolar current (Fig. 2a). The warmer conditions favor higher precipitation with a global pattern rather similar to what is found in future climate projections (Fig. 2b). This offset affects the mean climate state and is larger than the expected effect of Holocene dusts.

2.2 The IPSL Earth System Model and updated version of the land surface scheme

For these simulations, we use a modified version of the IPSLCM5A model (Dufresne et al., 2013). This model version couples the LMDZ.4 atmospheric model with 144x142 grid points in latitude and longitude (2.5°x1.27°) and 39 vertical levels (Hourdin et al., 2013) to the ORCA2 ocean model at 2° resolution (Madec, 2008). The ocean grid is such that resolution is enhanced around the equator and in the Arctic due to the grid stretching and pole shifting. The LIM2 sea-ice model is embedded in the ocean model to represent sea ice dynamics and thermodynamics (Fichefet and Maqueda, 1999). The ocean biogeochemical model PISCES is also coupled to the ocean physics and dynamics to represent the marine biochemistry and the carbon cycle (Aumont and Bopp, 2006). The atmosphere-surface turbulent fluxes are computed taking into account fractional land-sea area in each atmospheric model grid box. The sea fraction in each atmospheric grid box is imposed by the projection of the land-sea mask of the ocean model on the atmospheric grid, allowing for a perfect conservation of energy (Marti et al., 2010). Ocean-sea-ice and atmosphere are coupled once a day through the OASIS coupler (Valcke, 2006). All the simulations keep exactly the same set of adjusted parameters as in Dufresne et al. (2013) for the ocean-atmosphere system.

The land surface scheme is the ORCHIDEE model (Krinner et al., 2005). It is coupled to the atmosphere at each atmospheric model 30 min physical time steps and includes a river runoff scheme to route runoff to the river mouths or to coastal areas (d'Orgeval et al., 2008). Over the ice sheet water is also routed to

the ocean and distributed over wide areas so as to mimic iceberg melting and to close the water budget (Marti et al., 2010). This model accounts for a mosaic vegetation representation in each grid box, considering 13 (including 2 crops) plant functional types (PFT) and interactive carbon cycle (Krinner et al., 2005).

We made several changes in the land-surface model (Tab. 1). The first one concerns the inclusion of the 11 layer physically-based hydrological scheme (de Rosnay et al., 2002) that replaces the 2 layer bucket-type hydrology (Ducoudré et al., 1993). The 11 layer hydrological model had never been tested in the full coupled mode before this study. We gave specific care to the closure of the water budget of the land surface model to ensure that *O*(1000 years) simulations will not exhibit spurious drift in sea level and salinity. In addition the new prognostic snow model was included (Wang et al., 2013). The scheme describes snow with 3 layers that are distributed so that the diurnal cycle and the interaction between snowmelt and runoff are properly represented. In order to avoid snow accumulation on a few grid points, snow depth is not allowed to exceed 3m. The excess snow is melted and added to soil moisture and runoff while conserving water and energy (Charbit and Dumas, pers. communication). Because of a large cold bias in high latitudes in the first tests, we reduced the bare soil albedo that is used to combine fresh snow and vegetation in the snow aging parameterization. Other changes concern the adjustments of some of the parameterizations. The way the mosaic vegetation is constructed in ORCHIDEE favors too much bare soil when leaf area index (LAI) is low (Guimberteau et al., 2018). To overcome this problem, an artificial 0.70 factor was implemented in front of bare soil evaporation to reduce it (Table. 1). This factor is compatible with the order of magnitude of the reduction brought by the implementation of a new evaporation parametrization for bare soil in the current IPSLCM6A version of the model (Peylin pers. communication.). For all the other surface types the evaporation is computed as in L11. The last adjustment concerns the combination of snow albedo with the vegetation albedo. The procedure was different when vegetation was interactive or prescribed. Now, the combination of snow and vegetation albedo is based on the effective vegetation cover in the grid box in both cases. It leads to larger albedo than with the IPSL-CM5A-LR reference version when vegetation is prescribed. It counteracts the effect of the fresh snow albedo reduction.

2.3 Impact of the different changes on model climatology and performances

Figure 1 and 2 highlight how the changes discussed in section 2.2 affect the model adjustment and climatology. The hydrological model (L11) produces about 1.25 $mm.d^{-1}$ higher global annual mean evaporative rates than MH PMIP3. The water cycle is more active in L11. Precipitation is enhanced in the mid-latitudes and over the tropical lands (Fig. 2c) where larger evapotranspiration and cloud cover both contribute to cool the land surface (Fig. 2d). A higher evaporative rate should lead to a colder global mean temperature (Fig. 1c). This is not the case. The large scale cooling over land is compensated by warming over the ocean (Fig. 2d), caused by reduced ocean evaporation and changes in the ocean-land heat transport. The radiative equilibrium is achieved at the top of the atmosphere with the same global mean long wave and short wave radiation budget in the two simulations (L11 and MH-PI). The effect on precipitation is larger than the one due to the aerosol forcing discussed in section 2.1. The aerosol forcing induces mainly local thermodynamic changes. The effect of the L11 hydrology on evaporation induces larger changes in atmospheric circulation and thereby on precipitation.

The factor introduced to reduce bare soil evaporation didn't lead to the expected reduction of evaporation (Fig 1b). Indeed, when evaporation is reduced, soil temperature increases and the regional climate gets warmer allowing for more moisture in the atmosphere and thereby more evaporation where soil can supply

water (Fig. 2 e and f and Fig. 1). Therefore, differences resulting from bare soil evaporation do not show up on the precipitation map (Fig. 2 e) but on the increased temperature over land in the northern hemisphere (Fig. 1f). It is consistent with similar findings when analyzing land use feedback (Boisier et al., 2012). This stresses once more that fast feedbacks occur in coupled systems and that any comparison of surface fluxes should consider both the flux itself and the climate or atmospheric variables used to compute it (Torres et al., 2018). Note that in figure 2 f about 0.1°C of the 0.4°C global warming in L11AerEv is still a footprint of the warming induced by the aerosol effect described in section 2.1, but that it doesn't alter our conclusions on the regional temperature-evaporation feedback.

The difference between MH-FPMIP4 and MH-PMIP3 represents the sum of all the changes in the land surface model and forcing discussed above (Fig. 2 g and h). A PI simulation performed with the new model version (PI-FPMIP4, Tab. 1) allows us to assess how they affect the model performances. A rapid overview of model performances is provided by a simple set of metrics derived from the PCMDI Metric Package (Gleckler et al., 2016, see appendix 1). Figure 3 highlights that temperature biases are reduced in PI-PMIP4 at about all model levels but that biases are enhanced for precipitation and total precipitable water compared to PI-PMIP3 (comparison of blue and black lines in Fig. 3). Taken all together all the changes we made have little effect on the bias pattern (Fig. 3a). The model performs quite well compared to the CMIP5 ensemble of PI simulations, except for cloud radiative effect (Fig. 3). The effect of cloud in the IPSLCM5A-LR simulations has already been pointed out in several manuscripts and results mainly from low level clouds over the ocean (Braconnot and Kageyama, 2015; Vial et al., 2013). The atmospheric tuning is exactly the same as in the default IPSLCM5A-LR version, and the introduction of all the changes described above have almost no effect on the cloud radiative effect. Overall the model version with the 11 layer hydrology has similar skill as the IPSLCM5A reference (Dufresne et al., 2013) and we are confident that the version is sufficiently realistic to serve as a basis on top of which we can include the dynamical vegetation.

2.4 Initialization of the mid-Holocene dynamical vegetation for the transient simulation

We added the vegetation dynamics by switching on the dynamical vegetation model described in Zhu et al. (2015). Compared to the original scheme (Krinner et al., 2005), it produces more realistic vegetation distribution in mid and high latitude regions when compared with present-day observations.

Two different strategies have been tested to initialize the dynamical vegetation (Table 2). In the first case (MH-Vmap), the initial vegetation distribution was obtained from an off line simulation with the land surface model forced by CRU-NCEP 1901-1910 climatology. In the second case (MH-Vnone), the model restarted from bare soil with the dynamical vegetation switched on, using the same initial state as MH-Vmap for the atmosphere, the ocean, the sea-ice and the land-ice. As expected, the evolution of baresoil, grass and tree is very different between MH-Vmap and MH-Vnone during the first adjustment phase (black and blue curves in Fig. 4 a,b, and c). Vegetation adjusts in less than 100 years (1200 months) in MH-Vmap (blue curve). This short term adjustment indicates that the climate-vegetation feedback has a limited impact on vegetation when the initial state is already consistent with the characteristics of the simulated climate. In MH-Vnone that starts from baresoil (black curve), the adjustment has a first rapid phase of 50 years for bare soil and about 100 years for grass and tree, followed by a longer phase of about 200 years. The latter corresponds to a long term oscillation that has been induced by the initial coupling choc between climate and land surface. Note that PMIP4 instead of

PMIP3 MH boundary conditions were used to run the last part of these simulations (red and yellow curves in Fig. 4 a, b, and c). In the coupled system, most of the vegetation adjustment takes about 300 years, which is longuer than results of off line ORCHDEE simulations (less than 200 years). Since MH-Vnone started from a coupled ocean-atmosphere-ice state at equilibrium, this result also indicates that the land-sea-atmosphere interactions do not alter much the global energetics of the IPSL model in this simulation where atmospheric CO_2 is prescribed. The two simulations converge to very similar global vegetation cover. Figure 4 suggests that there is only one global mean stable state for the mid-Holocene with the IPSL model, irrespective of the initial vegetation distribution (see also Tab. A2, appendix A2).

For the transient simulations, we decided to use the results of the MH-VNone simulation as initial state (Table 2). We performed a preindustrial simulation (PI-Vnone) using MH-Vnone as initial state and switching on the orbital parameters and trace gases to their PI values. Figure 3 indicate that the vegetation feedback slightly degrades the global performances for PI temperature and bring the model performance close to the IPSLCM5A-LR CMIP5 version. It also contributes to reduce the mean bias in precipitable water, evaporation, precipitation and long wave radiation, but it has no effect on the bias pattern (assessed by the rmst in Fig. 3, see also appendix). Vegetation has thus an impact on climate, but this effect is smaller than those done to set up the model version we use here. Section 4 provides a more in depth discussion on vegetation state.

3 Simulated climate and vegetation throughout the mid to late Holocene

3.1 Long term forcing

Starting from the MH-Vnone simulation the transient simulation of the last 6000 years (TRHOLV) allows us to test the response of climate and vegetation to atmospheric trace gases and Earth's orbit (see section 2.1). The atmospheric CO_2 concentration is slowly rising throughout the Holocene from 264 ppm 6000 years ago to 280 for the pre-industrial climate around -100 BP (1850 CE) and then experiences a rapid increase from -100 BP to 0 BP (1950 CE) (Fig. 5). The methane curve shows a slight decrease and then follows the same evolution as CO_2, whereas NO_2 remains around 290 ppb throughout the period. The radiative forcing of these trace gases is small over most of the Holocene (Joos and Spahni, 2008). The largest changes occurred with the industrial revolution. The rapid increase in the last 100 years of the simulation has an imprint of about 1.28 $W.m^{-2}$.

The major forcing is caused by the slow variations of the Earth's orbital parameters that induce a long term evolution of the magnitude of the incoming solar radiation seasonal cycle at the top of the atmosphere (Fig. 5). It corresponds to decreasing seasonality in the northern Hemisphere and increasing seasonality in the southern Hemisphere (Fig. 5). It results from the combination of the changes in summer and winter insolation in both hemispheres (Fig. 6). These seasonal changes are larger at the beginning of the Holocene (about -8 $W.m^{-2}$ per millennia in the NH and +5 $W.m^{-2}$ per millennia in the SH) and then the rate of change linearly decreases in the NH (increases in the SH) from 4500 to about 1000 years BP. There is almost no change in seasonality in the NH over the last 1000 years, whereas in the SH seasonality starts to decrease again by 2000 years BP. The shape of insolation changes is thus different in both hemisphere, and so is the relative magnitude of the seasonal cycle between the two hemispheres. This would be seen whatever the calendar we use to compute the month means because of the seasonal asymmetry induced by precession at the MH (see: Joussaume and Braconnot, 1997; Otto-Bliesner et al., 2017).

3.2 Long term climatic trends

Changes in temperature and precipitation follow the long term insolation changes in each hemisphere and for the different seasons until about 2000 yrs BP to 1500 yrs BP (Fig. 6). Then trace gases and insolation forcing become equivalent in magnitude and small compared to MH insolation forcing, until the last period where trace gases lead to a rapid warming. The NH summer cooling reaches about 0.8 °C and is achieved in 4000 years. The last 100 year warming reaches 0.6 °C and almost counteracts, for this hemisphere and season, the insolation cooling. SH summer (JJAS) and NH Winter conditions (NDJF) are both characterized by a first 2000 years warming induced by insolation. It reaches about 0.4°C. It is followed by a plateau of about 3000 years before the last rapid increase of about 0.6°C that reinforces the effect of the Holocene insolation forcing. During SH winter temperature does not seem to be driven by the insolation forcing (Fig. 6 d). In both hemispheres summer precipitation trends correlate well to temperature trends, as it is expected from a hemispheric first order response driven by Clausius Clapeyron relationship (Held and Soden, 2006). This is not the case for winter conditions because one needs to take into account the changes in the large scale circulation that redistribute heat and energy between regions and hemispheres (Braconnot et al., 1997; Saint-Lu et al., 2016).

We further estimate the linkages between the long term climate response and the insolation forcing for the different latitudinal bands by projecting the zonal mean temperature and precipitation seasonal evolution on the seasonal evolution of insolation. We define the seasonal amplitude for each year as the difference between the maximum and minimum monthly values. We consider for each latitude the unit vector **S**:

$$\mathbf{S} = \frac{\mathbf{SW}_{is-TOA}}{\|\mathbf{SW}_{is-TOA}\|} \qquad (1),$$

where $\|\mathbf{SW}_{is-TOA}\|$ represents the norm of the seasonal magnitude of the incoming solar radiation at TOA over all time steps ($\boldsymbol{SW}_{is-TOA}$(t), *t*=-6000 years to 0, with an annual time step). Any climatic variable (**V**) can then be expressed as:

$$\mathbf{V}(\mathrm{t}) = \alpha(t)\mathbf{S} + \beta(t)\,\mathbf{b} \qquad (2),$$

with:

$$\alpha = \mathbf{V}.\mathbf{S} \qquad (3),$$

and **b** is the unit vector orthogonal to **S.** The ratio $\alpha/(\alpha+\beta)^{\frac{1}{2}}$ measure in which proportion a signal projects on the insolation (Figure 7). Figure 7 confirms that the projection of temperature and precipitation on the insolation curve is larger in the northern than in the southern hemisphere. The best match is obtained between 10°N and 40°N where about 80 % of the temperature signal is a direct response to the insolation forcing. The projections are only 40% in the tropics in the southern hemisphere. These numbers go up to 90% if a 100 year smoothing is applied to temperature. The seasonality precipitations project also to 90% when considering the filtered signal, confirming the strong linkages between temperature and precipitation in the NH over the long time scale. The projection is poorer, but not null, when the raw precipitation signal is considered. At the equator and in high latitudes in both hemispheres the projection is poor or null. At the equator, the MH insolation forcing favours a larger north/south seasonal march of the ITCZ over the ocean and the inland penetration of AfroAsian monsoon precipitation during boreal summer. Surface temperature is reduced in regions where precipitation is enhanced due to the combination of increased cloud cover and increased surface evaporation (Braconnot et al., 2007a; Joussaume et al., 1999). When monsoon retreats to its modern position, surface temperature in these regions increases, thereby enhancing its seasonal cycle. It is thus out of phase compared to the insolation forcing. This is

also true over SH continents where temperatures in regions affected by monsoons do not follow the local insolation and has similar seasonal evolution than the northern hemisphere. This out of phase relationship is consistent with glaciers reconstructions (Jomelli et al., 2011). In higher latitude the projection of the raw signal does not project well because of the large decadal variability. North of 40°N the mixed layer depth is also larger (about 200 m) than in the tropics (about 70m), which contribute to damp the seasonal change over the ocean. Thereby the seasonal temperature response is flatter than the shape of the seasonal insolation forcing, which lead to a poor projection over mid and high latitudes ocean especially in the ocean dominated SH (Fig. 7). Sea ice cover has also little change north of 80°N which also damps the changes in seasonality (Fig. 8). These changes are however amplified by the increase of sea ice during summer in the Artic resulting from cooler conditions with time, and by the reduction of the winter sea-ice cover in the Labrador and the Gin seas (Fig. 8a and b). For the snow cover the conditions are contrasted depending on the regions (Figure 8 b and d), with an increase decrease of the maximum cover over Eurasia related to long term rise of minimum temperature (Fig. 8 d)

3.3 Long term vegetation trends

These long term climate evolutions have a counterpart on the long term evolution of vegetation (Fig. 9). At the global and hemispheric scale, the long term vegetation trends correspond to reductions or increases of the area covered by vegetation reaching 2 to 4% of the total land area depending on vegetation type (Fig. 9). The global vegetation averages reflect the northern hemisphere changes where most of the vegetated continental masses are located. As expected from the different long term trend in insolation, the long term evolution of tree and grass covers are opposite between the two hemispheres. Note however that bare soil slightly increases in both hemispheres.

In the northern hemisphere the changes follow the changes in summer temperature, with the best match obtained for grass which increases almost linearly until 2000 years BP and then remains quite stable. In the southern hemisphere the phasing between vegetation change and temperature is not as good, again because this hemisphere is dominated by ocean conditions rather than land conditions. However, the tree expansion reaches a maximum between 2000 year BP and 1000 years BP and then the tree cover slightly decreases, which corresponds to the slight cooling in SH summer temperature. The gross primary productivity (GPP, Fig. 9 d) is driven in both hemispheres by the changes in tree cover. It accounts for a reduction of about 5 $PgCy^{-1}$. It is however possible that the GPP change is misestimated in this simulation because CO_2 is prescribed in the atmosphere, which implies that the carbon cycle is not fully interactive. Figure 10 compares the vegetation map obtained for the pre-industrial period in TRHOLV (50 years around 1850 AC, which corresponds to 150 - 100 years BP) with MH vegetation. It shows that bare soil increases in semi-arid regions in Africa and Asia, as well as in South Africa and Australia. The reduction in tree PFTs is maximum north of 60°N, in South and Southeast Asia, Sahel and most of North America. They are replaced by grass PFTs. In the southern hemisphere forest cover increases in South Africa, South East South America and part of Australia.

In the last 100 years the effect of trace gases and in particular the rapid increase of the atmospheric CO_2 concentration leads to a rapid vegetation change characterized by tree regrowth, which is dominant in the NH (Fig. 9 and 10). This tree recovery counteracts the reduction from mid Holocene in mid and high NH latitudes (Fig. 10 b, e, and h). This effect is consistent with the observed historical growth in gross primary production discussed by Campbell et al. (2017). The GPP increase in the last 100 years results from increased atmospheric

CO_2. It suggests that the CO_2 effect counteracts the tree decline induced by insolation. When reaching 0k BP (1950 CE), bare soil remains close to PI, grass reduces by 3% and tree increases by about 3%.

3.4 Regional trends

Figure 11 highlights the long term vegetation trends for three regions that respectively represent climate conditions north of 60°N, over the Eurasian continent, and in the West African monsoon Sahel/Sahara region. These are regions for which there are large differences in MH – PI climate and vegetation cover (Fig. 9 and 10). They have also been chosen because they are widely discussed in the literature and are also considered as tipping points for future climate change (Lenton et al., 2008). They are well suited to provide an idea of different characteristics between regions.

North of 60°N and in Eurasia a substantial reduction of tree at the expense of grass starts at 5000 years BP (Fig. 11 a and b). Vegetation has almost its pre-industrial conditions around 2500 years BP. The largest trends are found between 5000 years BP and 2500 years BP in this region and this reflects well the timing of the NH hemisphere summer cooling. The change in total forest in Eurasia is small. A first change is followed by a second one around 3000 years BP. Despite the 100 year smoothing applied to all the curves, they exhibit large decadal to multi centennial variability. Over West Africa (Fig. 11 c), the largest trends start slightly later (4500-5000 years BP) and are more gradual until 500 years BP. The vegetation trends are also punctuated by several centennial events that do not alter much the long term evolution as some of these events do in the other two boxes.

The variability found for vegetation is also found in temperature and precipitation at the hemispheric scale (Fig. 6). It is even higher at the regional scale in mid and high latitudes (Fig 8). This variability is not present in the imposed forcing. It results from internal noise. Because of this it is difficult for example to say if the NH hemisphere winter temperature trend was rapid until 4000 years BP and then temperature remains stable, or if the event impacting temperature and precipitation around 4800 to 4500 BP masks a more gradual increase until 3000 BP as it is the case for NH Summer where the magnitude of the temperature trend is larger than variability (Fig. 6). Note that some of these internal fluctuations reach half of the total amplitude of the regional vegetation trends (Fig. 11), and that it is a dominant signal over Eurasia, where the long term mean change in the total tree cover is small (Fig. 10 and 11). Temperature and precipitation are well correlated at this centennial time scale (Fig. 6).

Despite the dry bias over the Sahel region in this version of the model, the timing of the vegetation changes over West Africa reported in figure 11 is consistent with the major features discussed for the end of the African humid period (Hély and Lézine, 2014; Liu et al., 2007). In particular, the replacement of grass by bare soil starts earlier than the reduction of the tree cover located further south (Fig. 11). At the scale of the Sahel region, we do not have abrupt but gradual changes in vegetation. It is however abrupt at the grid cell level. These changes are associated with the long term decline of precipitation, as well as the southward shift of the tropical rain belt associated with the African monsoon (Fig. 12). The location (latitude) of the rain belt is estimated here as the location of the maximum summer precipitation zonally averaged between 10°W and 20°E over West Africa. Most of the southward shift of the rain belt occurs between MH and 3500 years BP and correspond to a difference of about 1.8°N of latitude over this period. Then the southward shift is smaller, with a total shift of 2.5°N of latitude diagnosed in this simulation. The comparison of figure 11 and 12 clearly shows that the rapid

decrease of vegetation occurs after the rapid southward shift of the rain belt. An interesting point is that the amount of precipitation is also shifted in time compared to the location of the rain belt. It suggests that the vegetation feedback on precipitation is still effective during the first period of precipitation decline and that it might have amplify the reduction of precipitation when vegetation is reduced over the Sahel region.

As seen in figure 10, the NH decrease in forest cover is mainly driven by the changes that occur north of 60°N (Fig. 8 and 10). These trends reflect more or less what is expected from observations (Bigelow et al., 2003; Jansen et al., 2007; Wanner et al., 2008). It results from the summer cooling that affects both the summer sea-ice cover in the Artic, the summer snow cover over the adjacent continent and the amplification of the insolation forcing south of 70°N by snow/vegetation albedo feedback. Further south over Eurasia, figure 11 suggests that there are only marginal changes in Eurasia in terms of vegetation. Figure 13 shows the total tree cover over this region does not reflect well the mosaic vegetation and forest composition. Indeed, the long term decrease in forest is dominated by the decrease in temperate and boreal deciduous trees. Boreal needle leaf evergreen trees do not change whereas the temperate ones increase. This figure also highlights that the long term change in Eurasian tree composition throughout the mid to late Holocene is punctuated by centennial variability. The different trees have also different timing and variability. Boreal forests are more sensitive to variability during the first 3000 years of the simulation, whereas, temperate broadleaf tree exhibit larger variability in the second half. The large events have a climatic counterpart (Fig. 8), so that the composition of the vegetation is a result of a combined response to the long term climatic change and to variability. These two effects can lead to different vegetation composition depending on stable or unstable vegetation states (Scheffer et al., 2012). Decadal vegetation changes have been discussed for recent climate in these regions (Abis and Brovkin, 2017), which suggests that despite the fact that our dynamical vegetation model might underestimate vegetation resilience, the rapid changes in vegetation mosaic is a key signal over Eurasia. Future model data comparisons should consider composition changes and variability to properly discuss vegetation changes over this region.

4 Vegetation, uncertainties and multiple vegetation states

4.1 Simulated versus reconstructed vegetation

Section 3 shows how climate and vegetation respond to insolation and trace gases. The simulated changes are in broad agreement with what is expected from various sources of data. However, section 2 mentions model adjustments and biases. They all contribute to the difficulty to produce the right vegetation changes at the right place, at the right time and for the right reasons. It is thus important to fully understand what we can expect in terms of realism from this simulation. We investigate it for the mid-Holocene and modern climate for which we can use the BIOME6000 vegetation reconstruction (Harrison, 2017).

The dynamical vegetation module simulates fractional cover of 13 PFTs. These PFTs cannot be directly compared with the reconstructed biome types based on pollen and plant macrofossil data from the BIOME 6000 dataset (Harrison, 2017). In order to facilitate the comparison, we converted the simulated PFTs into eight mega-biomes, using the biomization method algorithm proposed by Prentice et al. (2011). The algorithm uses a mixture of simulated climate and vegetation characteristics (see appendix and Fig. A2). Alternative thresholds as proposed in previous studies (Joos et al., 2004; Prentice et al., 2011) were tested to account for the uncertainties in the biomization method (see Fig. A2). At first look MH-Vnone reproduces the large scale pattern found in the

BIOME6000 reconstruction (Fig. 14a). The comparison however indicates that the boreal forest tree line is located too far south. It results from a combination of a cold bias in temperature in these regions and a systematic underestimation of forest biomass in Siberia with ORCHIDEE when forced by observed present-day climate (Guimberteau et al., 2018). Such underestimation of tree biomass could lead to too low tree height in ORCHIDEE, and thus to the replacement of boreal forest by dry woodland according to the biomization algorithm (Fig. A2a). Also, vegetation is underestimated in West Africa, consistent with a dry bias (not shown). The underestimation of the African monsoon precipitation is present in several simulations with the IPSL model (Braconnot and Kageyama, 2015), and is slightly enhanced in summer when the dynamical vegetation is active. With interactive vegetation however equatorial Africa is more humid (Fig. 15a). Figure 14c provides an idea of the major mismatches between simulated vegetation and the BIOME6000 reconstructions. In particular the simulation produces too much desert where we should find grass and shrub. It also produces too much tundra instead of boreal forest, and too much savanah and dry woodland in several places that should be covered by temperate-tree, boreal-tree or tundra, confirming the visual map comparison (Fig. 14c). Similar results are found when considering the pre-industrial climate in TRHOLV compared to the BIOME6000 pre-industrial biome reconstruction (see Fig. A2 d). These are systematic biases. These systematic biases are confirmed when comparing the simulated PFTs for PI with those of the 1860 PI map estimated from observations and used in simulations with prescribed vegetation (see Tab. A2 for regions without land use).

It is not possible to estimate the vegetation feedback on the long term climate evolution from the transient simulation. It is however possible to infer how the dynamical vegetation affects the mean climatology for the MH, period for which simulations with prescribed and dynamic vegetation are available. Metrics discussed in section 2.4 (Fig. 3) show that the introduction of the dynamical vegetation in the model reduces the amount of precipitation and that the climate is dryer. The simulations with dynamical vegetation only consider natural vegetation, whereas the 1860 map we prescribe when vegetation is fixed include land use. In regions affected by land use all MH simulations produce less baresoil (3%), more tropical trees (5%), similar temperate tree cover, increased boreal tree cover (10%) and a different distribution between C3 versus C4 grass (see Tab. A2). In Eurasia where croplands are replaced by forest, the lower forest albedo induces warmer surface conditions (Figure 15 b). Also, when snow combines with forest instead of grasses, the snow/vegetation albedo is lower leading to the positive snow-forest feedback widely discussed for the last glacial inception (de Noblet et al., 1996; Kutzbach et al., 1996). Figure 15a also highlights that precipitation is increased over the African tropical forest and reduced over South America. In most regions the impact of vegetation is much smaller that the impact of the changes in the land surface hydrology and forcing strategy discussed in sections 2.3 (Fig. 2).

The differences between the MH simulated vegetation map and the 1860 PI map reflect both systematic model biases and vegetation changes related to the MH climate differences with PI. We can infer from figures 15 and 16 that vegetation has a positive warming feedback in the high latitudes during MH. Part of the differences between the MH and the PI conditions in figure 15 c and d are dominated by the impact of vegetation. Similar patterns as those obtained for the impact of vegetation are found over Eurasia for temperature, or south East Asia and North America for precipitation. For the grid points where BIOM6000 data are available for both MH and PI (0k), the major simulated biome changes occur for Savana&Wood and Grass &Shrub (Fig. 14 e). Differences are also found for tree and tundra, to a lesser extent. The comparison with similar estimates from BIOME6000 reconstructions indicates that Grass &shrub exhibit the major changes and that tree show larger differences

compared to the simulation. The model shift between Savana&Wood and Grass &shrub is consistent with the noted bias for Savana and the fact that the tree cover is underestimated in norther NH latitudes (Fig. 14).

Note that the vegetation differences found between the historical period and the PI period in TRHOLV are not negligible. We can estimate from figure 15 a and b that neglecting land use leads to an underestimation of about 1°C in Eurasia between the MH and PI in this TRHOLV simulation. Depending if PI or the historical period is used as reference the magnitude of the MH changes in vegetation and climate would be different. Also land use has regional impacts and should be considered in PI or in the historical period. This stresses that quantitative model-data comparison should be considered with care, knowing that both the reference period (PI or historical) and the complexity of the land surface model (prescribed vegetation, natural dynamical vegetation, land use...) can easily lead to 1°C difference in some regions.

4.2 Multiple vegetation states for the pre-industrial climate

Another source of uncertainty concerns the stability of the simulated vegetation maps. Several studies suggest that the initial state has only minor impact on the final climate because there is almost no changes in the thermohaline circulation over this period and models do not exhibit major climate bifurcations (e.g. Bathiany et al., 2012). This is the main argument used by Singarayer et al. (2010) to justify that their suite of snap shot experiments may provide reasonable transient climate vision when put together. Is it the case in the TRHOLV simulation when vegetation is fully interactive? This transient simulation does not exhibit much change in indices of thermohaline circulation that remains close to 16-18 Sv (1 Sv = $10^6 m^3.s^{-1}$) throughout the period. The global metrics (Fig. 3) show that at the global scale the results of the TRHOLV simulations for PI (around 100 BP = 1860 AC) are similar to those of PI-Vnone. It is also the case for seasonal and extratopical/tropical values (Fig. A1). We can therefore conclude that there is no difference in mean surface climate characteristics between the snap shot PI-Vnone experiments and the PI period simulated in transient TRHOLV simulation.

Then, is the vegetation also similar to the one simulated in PI-VNone? The PI vegetation simulated in TRHOLV shows little differences to the one found for PI-Vnone (Fig. 10 c, f, and i). The relative percentages of land covered by the different vegetation classes correspond to 15% for bare soil, 41% for grass and 43% for tree respectively. These values are similar to the one found for PI-VNone (15%, 40% and 44% respectively) within 1% error bar. This doesn't necessarily hold at the regional scale where regional differences are also found between PI-THROLV and PI-Vnone. Indeed, figure 10 indicates differences in tree and grass cover in Eurasia around 60°N and different geographical coverage between bare soil, grass and trees over South Africa and Australia. These differences are very small compared to the differences between MH and PI in TRHOLV, but are as large as the difference between hist and PI in a few places in Eurasia. As seen in previous section, these are regions where variability is large and vegetation instable.

We also tested if the PI vegetation and climate would also be similar when starting from MH-Vmap instead of MH-Vnone (dark pink and orange lines in Fig. 4d, e and f). This is also a way to have a better idea of the range of response one would expect from ensemble simulations, knowing that we only ran one full transient simulation. For the PI-Vmap simulation, the orbital parameters and trace gases were first prescribed to pre-industrial conditions for 15 years while maintaining the vegetation PFTs in each grid cell to those obtained in MH-Vmap (Tab. 2, Fig. 4). Then, the dynamical vegetation was switched on. It induces a rapid transition of the

major PFTs that takes about 10 years before a new global equilibrium is reached (Fig. 4 d, e and f). For PI-VNone presented in section 2.4 the same procedure was applied, but the dynamical vegetation was switched on after 5 years (Tab. 2 and Fig. 4), and the new equilibrium state is reached without any relaxation or rapid transition.

PI-Vnone and PI-Vmap converge to different global vegetation states (Fig. 4). Compared to the values listed above for PI-Vnone and PI-TRHOLV the respective covers of bare soil, grass and tree for PI-Vmap are 20%, 37% and 43%. In particular PI-Vmap produces a larger bare soil cover than PI-Vnone (Fig. 4 d). It is even larger than the total bare soil cover found in the 1860 CE map used in PI simulations when vegetation is prescribed (Fig. 4). Interestingly part of these differences between Vmap and Vnone, are found in the southern hemisphere and the northern edge of the African and Indian monsoon regions. These differences in PI vegetation explain the vegetation differences between MH and PI (Fig. 16), and mainly concern the distribution between grass and bare soil. The simulated changes seem larger with Vmap. Previous assessment of model results against vegetation and paleoclimate reconstructions (e.g. Harrison et al., 2014; Harrison et al., 1998) suggest that MH – PI vegetation for Vmap would look in better agreement with reconstructed changes from observations in terms of forest expansion in the northern hemisphere or grasses in Sahel (Fig. 16). However, the modern vegetation map for this PI-Vmap simulation has even less forest than PI-Vnone north of 55°N (Fig. 4 e, f and i), for which forest is already underestimated (Fig. A2). These differences in PI vegetation have only a small counterpart in climate. It corresponds to cooler condition in the mid and high norther latitude (Fig. 15). In annual mean there is almost no impact on precipitation (Fig. 15). In terms of climate these two simulations are very similar, and closer to each other than to other simulations, whatever the season or the latitudinal band (see figure A1). The small differences in climate listed above are thus too small to be captured by global metrics. It suggests that there is no direct relationship between the different vegetation maps and model performances. The different vegetation maps are obtained with a similar climate, which indicates that in this model multiple global and vegetation states are possible under pre-industrial climate or that tiny climate differences can lead to different vegetation.

5 Conclusion

This long transient simulation over the last 6000 years with the IPSL climate model is one of the first simulations over this period with a general circulation model including a full interactive carbon cycle and dynamical vegetation. We show that, despite some model biases that are amplified by the additional degree of freedom resulting from the coupling between vegetation and climate, the model reproduces reasonably well the large scale features in climate and vegetation changes expected from the observation over this period. There has been lots of discussion on the sign of the trends in the northern mid-latitude following the results of the first coupled ocean-atmosphere simulation with the CCSM3 model across the deglaciation. Our results seem in broad agreement with the 6000 to 0 part of the revised estimates by Marsicek et al. (2018). There is little change in annual mean climate throughout the last 6000 years (not shown). The seasonal cycle is the main driver of the climate and vegetation changes, except in the last part of the simulation when the rapid greenhouse gas concentration increase leads to a rapid global warming.

Several points emerge from this study. The first one is that the MH-PI changes in climate and vegetation is similar in our simulation between snapshot experiments and a long transient simulation. What is the value added then of the transient simulation? The good point is that model evaluation can be done on snapshot

experiments, which fully validate the view that the mid-Holocene is a good period for model benchmarking in the Paleoclimate Modeling Intercomparison Project (Kageyama et al., 2018). However the MH – PI climate conditions mask the long term history and the relative timing and the rate of the changes. The major changes occur between 5000 and 2000 year BP and the exact timing depends on regions. In our simulation the forest reduction in the northern hemisphere starts earlier than the vegetation changes in Africa. It also ends earlier. The last period reflects the increase in trace gases with a rapid regrowth of tree in the last 100 years when CO_2 and temperature increase at a rate not seen over the last 6000 to 2000 years. Some of these results already appear in previous simulations with intermediate complexity models (Crucifix et al., 2002; Renssen et al., 2012). Using the more sophisticated model with a representation of different types of tree brings new results. Even though the total forest cover does not vary much throughout the Holocene in TRHOLV, the composition of the forest varies more substantially, with different relative timing between the different PFTs.

We mainly consider here surface variables that have a rapid adjustment with the external forcing. Also, we only consider long term trends in this study, but the results highlight that centennial variability plays an important role to shape the response of climate and vegetation to the Holocene external forcing at regional scale. In depth analyses of ice covered regions and of the ocean response would be needed to tell wether the characteristics of variability depends or not on the pace of climate change. It would guide the development of methodologies to assess the vegetation instabilities as the one seen in Eurasia. They might share some similarities with the vegetation variability reported in this region for the recent period (Abis and Brovkin, 2017). These simulations offers the possibility to analyze the simulated internal instability of vegetation that could be partly driven by climate noise (Alexandrov et al., 2018). The different time scales involved in this long term evolution can be seen as an interesting laboratory for further investigation in this respect.

The vegetation differences between PI-Vmap and PI-VNone raise once more the possibility for multiple vegetation equilibrium under pre-industrial or modern conditions as it has been widely discussed previously (e.g. Brovkin et al., 2002; Claussen, 2009). Here we have both global and regional differences. Our results are however puzzling, because we only find limited differences between the PI-Vnone snapshot simulation and the PI climate and vegetation produced at the end of TRHOLV. These simulations start from the same initial state and in one case PI condition are switch on in the forcing, whereas the other case the 6000 years long term forcing in insolation and trace gases is applied to the model. An ensemble of simulations would be needed to fully assess vegetation stability. In the northern hemisphere and over forest areas, MH-Vmap produced slightly less trees that MH-Vnone. It might have been amplified by snow albedo feedback under the PI conditions that are characterized by a colder than MH climate in high latitudes in response to reduced incoming solar radiation associated with lower obliquity. The differences between the southern and northern hemisphere characterized by large differences in grasses and bare soil are more difficult to understand and suggest different response to the changes in southern hemisphere seasonality. This is in favor of different equilibrium induced only partly by climate-vegetation feedback. We need also to raise the point that there is still a very small probability that these differences come from inconsistent modeling when vegetation is prescribed or when we use the dynamical model. This should not be the case because it would not explain why vegetation is sensitive to initial state in PI and not in MH. It is also possible that the climate instability induced by the change from one year to the other in insolation and trace gases leads to rapid amplification of climate in high latitude, which is more effective under

the cooling high latitude condition found in PI. The strongest conclusion from these simulations is that the vegetation-climate system is more sensitive under the pre-industrial conditions (at least in the NH latitudes).

This study also points out the difficulties to fully assess model results. Part of it is due to model biases that prevent the simulation to be correct at regional scale, or where data are available. Specific methodology needs to be developed for model-data comparison designed to assess the climate-vegetation dynamics over a long time scale without putting too much weight on inherent model biases. There is also an intrinsic reason related to the fact we only represent natural vegetation, and neglect land use and also aerosols other than dust and sea-salt. Therefore the PI and historical climate cannot be realistically reproduced, even though most of the characteristics we report are compatible with what has been observed. Our results also show that the assessment of the magnitude of the simulated differences between MH and modern conditions depends on the reference period. This has implication for model-data comparisons, but also for reconstruction of temperature or moisture from paleoclimate archives that are in general calibrated using specific datasets. Similar methodologies for data sampling need thus to be applied both on paleoclimate records and on model outputs. It also suggests that more needs to be done to derive criteria allowing us to assess the processes leading to the observed changes rather than the changes themselves.

6 Appendix

6.1 A1 Spatio-temporal agreement between model results and observations in the extratropics and tropics

Figure 3 highlights the model-observation agreement for the pre-industrial climate considering global metrics, commonly used to evaluate model climatology. The mean bias ($Bias_{xy}$) represents the difference between the spatio-temporal averages of a simulated variable with observations. Here all metrics consider fifty year averages from observations or reanalysis products. We estimate the spatio-temporal mean of each variable as:

$$\mathrm{Var}_{xy} = \frac{1}{T}\sum_{i,j,t} w_{i,j} Var_{i,j,t} \quad (4)$$

Where $w_{i,j}$ (with $\sum_{i,j} w_{i,j} = 1$) represents the ratio of the surface of the grid-cell to the total surface of the grid, and T the number of time steps. If we call *Var_mod* the simulated variable and *Var_obs* the observed one, the mean bias expressed as

$$Bias_{xy} = \mathrm{Var\_mod}_{xy} - Var\_obs_{xy} \quad (5)$$

measures the mean difference over the whole spatial domain and all time steps (12 climatological months).

The RMSE (rms_{xyt}) is the Root Mean Squared Error computed between the model and the reference over the twelve climatological months:

$$rms_{xyt} = \sqrt{\frac{1}{T}\sum_{i,j,t} w_{i,j}\,(Var\_mod_{i,j,t} - Var\_obs_{i,j,t})^2} \quad (6)$$

The metric is sensitive to the value of the mean bias, and provides a measure of the spatio-temporal agreement between the model and the reference.

We present the global metrics only in the main text (see figure 3). We complete the analyses by computing the same metrics (bias and root mean square) at the seasonal time scale and for 3 latitudinal bands. We restrict the figure to surface air temperature and precipitation that reflects well the major differences. It shows that these measures capture differences between the IPSLCM5A-LR version of the IPSL model (Dufresne et al., 2013) and the new version developed for the TRHOLV transient simulation (see section 2). It also highlights the impact of running the model with the dynamical vegetation. However, as in Figure 3 the simulations with different MH conditions for the interactive vegetation, as well as the PI conditions obtained after 5900 years of transient simulation are difficult to distinguish. Differences become significant again when considering the last 50 years of the transient simulations that are affected by increase greenhouse gases.

6.2 A2 Biomization and sensitivity analysis.

Table A2 show the different ORCHIDEE PFT for the different MH and PI simulations, considering the regions that are affected, or regions that are not affected by land use in the pre-industrial simulation with vegetation prescribed to the 1860 observed values.

	regions with landuse				**regions without landuse**							
PFT	MH TRHOLV	MH Vnone	MH Vmap	PI 1860	MH TRHOLV	MH Vnone	MH Vmap	PI TRHOLV	PI Vnone	PI Vmap	PI 1860	Hist TRHOLV
1 - Bare soil	9	9	8	12	21	22	22	24	23	28	26	23
2 - tropical broad-leaved evergreen	15	15	15	13	5	5	5	5	5	5	8	5
3 - tropical broad-leaved raingreen	8	8	8	11	3	3	3	3	3	3	2	3
4 - temperate needleleaf evergreen	8	8	8	5	1	1	1	1	1	1	2	1
5 - temperate broad-leaved evergreen	4	4	4	6	1	0	0	1	1	1	3	1
6 - temperate broad-leaved summergreen	9	8	8	8	2	2	2	2	2	2	2	2
7 - boreal needleleaf evergreen	9	9	9	2	13	13	11	8	10	9	8	11
8 - boreal broad-leaved summergreen	3	3	3	1	4	5	4	3	3	3	8	3
9 - boreal needleleaf summergreen	1	1	1	0	4	4	4	3	3	2	4	3
10 - C3 grass	17	17	16	23	37	36	36	41	41	39	32	38
11 - C4 grass	18	18	20	13	10	10	12	10	9	8	5	10
12 - C3 agriculture	0	0	0	4	0	0	0	0	0	0	0	0
13 - C4 agriculture	0	0	0	2	0	0	0	0	0	0	0	0

Table A2. Distribution of ORCHIDEE 13 PFTs (%) in different simulations and the PI 1860 map used as boundary conditions when vegetation is prescribed from pre industrial observations. If the PI 1860 fraction of land use in a grid box is larger than 0.01 then the grid box is considered as covered with land use. The percentage is computed for each region separately, each region having its own total area. The error bars are about 0.5, which is accounted for in the table by neglected decimals in the estimates.

To convert the ORCHIDEE model PFTs into mega biomes we use the algorithm proposed by Prentice et al. (2011) and used by Zhu et al. (2018). Figure A2a shows the different thresholds used in the algorithm. The black numbers correspond to the default values used to produce figure 14 in the main text. Since some of these thresholds are somehow artificially defined, we also tested the robustness of our comparison by running sensitivity tests. These tests considered successively different threshold in Growing Degree Days above 5°C (GDD5), canopy height and foliage projective cover as indicated in red on figure A2a.

The different thresholds induce only slight difference on the biome map for a given simulation. The largest sensitivity is obtained for the height. When 10 m is used instead of 6 m, a larger cover of savannah and dry woodland is estimated from the simulations in mid and high northern latitudes. In these latitudes also, a large sensitivity is found when the GDD5 limit is set to 500°C. d^{-1} instead of 350°C.d^{-1} between tundra and savannah and dry woodland or boreal forest.

The same analyses transformation into megabiomes was performed for the Vmap and Vnone simulations. Similar sensitivity is found to the different thresholds for these two simulations (Fig. A2 b). The synthesis of the goodness of fit between model and data is presented in figure A2 c. It shows that the two simulations provide as expected very similar results when compared to the MH BIOME6000 map. It is interesting to note that the different thresholds do not have a large impact on the model data comparison, when all data points are considered. The change in GDD5 limit produces tundra in better agreement with pollen data, and the canopy height better results with savannah and dry woodland. Note however that this result is in part due to the fact that there is little data in regions where the impact is the largest (Figure 6 in the main text).

The same procedure was also applied to the PI Vnone and PI-Vmap simulations. The overall correctness (percentage of reconstruction sites showing the same megabiome between model and data) is similar as the one obtained for MH (37% for MH and 35% for PI). These numbers are close to the percentages derived by Dallmeyer et al. (2019) using a climate-based biomization method (i.e. use ESM modeled climate states to force a biogeography model to simulate the biome distribution), which gives 33% and 39% with two IPSL model versions for pre-industrial

Acknowledgments. We would like to thanks our colleagues from the IPSL global climate model group for their help in setting up this intermediate version of the IPSL model. In particular the ORCHIDEE group provided good advices for the closure of the hydrological cycle in the land surface scheme (Philippe Peylin, Agnès Ducharne, Fréderic Cheruy and Joséfine Gattas) or the snow ablation (Sylvie Charbit and Christophe Dumas). The workflow for these long simulations benefits from the development of Anne Cozic and Arnaud Caubel. Discussions with Philippe Ciais and Yves Balkansky were also at the origin of the choice of the land surface model complexity and aerosols forcing strategy. We acknowledge PRACE for awarding us access to Curie at GENCI@CEA, France (THROL project) to start the simulations. The simulations were also performed using HPC resources from GENCI-TGCC thanks to a high end computing access grant and to our annual allocation time (gen2212). This work is supported by the JPI-Belmont PACMEDY project (**N ° ANR-15-JCLI-0003-01).**

Simulation	Comment	Initial state
Reference MH) simulations with prescribed vegetation map		
MH_PMIP3	Reference PMIP3-CMIP5 IPSL simulation (Kageyama et al., 2013a)	Previous MH long term simulation with the model used to test model configuration
MH_FPMIP4 (S_Sr04)	Reference version used here, with vegetation prescribed to the 1860 vegetation map as in PMIP3-CMIP5.	From year 250 of MH_L11AerEv below
Reference PI simulations with prescribed vegetation map		
PI_PMIP3	Reference PMIP3-CMIP5 IPSL simulation (Dufresne et al., 2013; Kageyama et al., 2013a)	
PI_FPMIP4	As L11AerEV but with pre industrial trace gases and Earth's orbital parameters	
MH sensitivity experiments with prescribed vegetation map		
MH_L11 (S_Sr01)	As PMIP3, but with new version of land surface model (hydrology and snow model	From the last MH test of the new model configuration (new version of ORCHIDEE)
MH_L11Aer (S_Sr02)	As L11, but only dust and sea-salt considered in the aerosol forcing	Same as L11
MH_L11AerEv (S_Sr03)	As L11aer, but with factor to limit bare soil evaporation	From year 250 of L11Aer

Table 1. Tests done to set up the model IPSL version in which we included the dynamical vegetation. For all these simulations the vegetation map is prescribed to the 1860 map used in PI-PMIP3. The different columns highlight the name of the test and the initial state to better isolate the different factors contributing to the adjustment curves in Figure 1. We include in parenthesis the tag of the simulation that corresponds to our internal nomenclature for memory.

Simulation	Comment	Initial state
Reference Mid Holocene (MH) and PI simulations with dynamical vegetation		
MH-Vnone (V-Sr09)	L11AerEv configuration but initial state with bare soil everywhere	Year 250 of L11Aer for atmosphere ocean and sea ice
MH-Vnone_FPMIP4 (V-Sr12)*	Same simulation as MH-Vnone, but using the PMIP4 trace gases forcing	Year250 of MH-Vnone for all model components
PI-Vnone (V_Sr12) *	Preindustrial simulation corresponding to the MH simulations starting from bare soil	Year 500 of MH-Vnone-FPMIP4 for all model components
Refence transient simulation of the last 6000 years with dynamical vegetation		
TRHOLV	Transient mid Holocene to present day simulation with dynamical vegetation	Year 500 of MH-Vnone-FPMIP4 for all model components
Sensitivity experiments to dynamical vegetation		
MH-Vmap (V_Sr10)	As L11AerEv, but vegetation map and soil initial state from an off line ORCHIDEE vegetation force with L11 pre-industrial simulation	Year 250 or L11AerEv for atmosphere, ocean and sea-ice
MH-Vmap_FPMIP4 (V_Sr11)	Same simulation as MH-Vmap, but using the PMIP4 trace gases forcing	Year 200 of MH-Vmap, for all model components
PI-Vmap (V_Sr07)	Preindustrial simulation corresponding to the MH simulation starting from the off line ORCHIDEE vegetation force with L11 pre-industrial simulation	Year 250 of Vmap_FPMIP4, for all model components.

Table 2. Simulations run to initialize the dynamical vegetation starting from bare soil or from vegetation map and soil moisture resulting from an off line ORCHIDEE simulation with dynamical vegetation switch on and using the PI L11 simulated climate as boundary conditions. Simulations with an * are considered as references for the model version and the transient simulations. We include in parentheses the tag of the simulation that corresponds to our internal nomenclature for memory.

7 Figure Caption

Figure 1: Illustration of the effect of the different adjustments made to produce mid-Holocene simulations with the modified version of the IPSLCM5A-MR version of the IPSL model in which the land surface model ORCHIDEE includes a different soil hydrology and snow models (see text for details). The three panels show the global average of a) net surface heat flux ($W.m^{-2}$), b) evaporation ($kg.m^{-2}$), and c) 2m air temperature (°C). The different color lines represent the results for the different simulations reported in Table 1.

Figure 2: Mid Holocene annual mean precipitation ($mm.d^{-1}$) and 2m air temperature (°C) differences between a) and b) L11Aer and L11, c) and d) L11 and PMIP3, e) and f) PMIP3L11AerEv and L11Aer, and g) and h) FPMIP4 and PMIP3. See Table 1 and text for the details about the different simulations.

Figure 3. a) Annual mean global model bias (bias_xy) and b) spatio-temporal root mean square differences (rms_xyt) computed on the annual cycle (twelve climatological months) over the globe for the different pre-industrial simulations considered in this manuscript (colors lines) and individual simulations of the CMIP5 multi-model ensemble (grey lines). The metrics for the different variables are presented as parallel coordinates, each of them having their own vertical axis with corresponding values. In these plots, ta stands for temperature (°C) with s for surface, 850 and 200 for 850 and 300 hPa respectively, prw for total water content ($g.kg^{-1}$), pr for precipitation ($mm.d^{-1}$), rlut for outgoing long wave radiation ($W.m^{-2}$), rltcre and rltcre for the cloud radiative effect at the top of the atmosphere in the short wave and long wave radiation respectively ($W.m^{-2}$). See annex A1 for details on the metrics.

Figure 4. Long term adjustment of vegetation for a), b), and c) mid Holocene (MH) and c), d) and e) preindustrial (PI) climate, when starting from bare soil (Vnone) or from a vegetation map (Vmap). The 13 ORCHIDEE PFTs have been gathered as bare soil, grass, tree and land-use. When the dynamical vegetation is active only natural vegetation is considered. Land-use is thus only present in one simulation, corresponding to a pre-industrial map used as reference in the IPSL model (Dufresne et al. 2013). The corresponding vegetation is referred to as PI_prescribed. The x axis is in months, starting from 0, which allows to plot all the simulation that have their own internal calendar on the same axis.

Figure 5: Evolution of trace gases: CO_2 (ppm), CH_4 (ppb) and N_2O (ppb), and seasonal amplitude (maximum annual – minimum annual monthly values) of the incoming solar radiation at the top of the atmosphere ($W.m^{-2}$) averaged over the northern (black line) and the southern (red line) hemispheres. These forcing factors correspond to the PMIP4 experimental design discussed by Otto-Bliesner et al. (2017).

Figure 6. Long term evolution of incoming solar radiation at the top of the atmosphere (TOA)(Wm^{-2}, top panel) and associated response of temperature (°C) and precipitation ($mm.y^{-1}$) expressed as a difference with the 6000 year PB initial state and smoothed by a 100 year running mean) for a) NH Summer, b) NH winter, c) SH summer, and d) SH winter. Temperatures are plotted in red and precipitation in blue for summer, and they are respectively plotted in orange and green for winter. NH Summer and SH Winter correspond to June to September averages whereas NH winter and SH summer correspond to December to March averages. All curves, except insolation, have been smoothed by a 100 year running mean.

Figure 7: Fraction of the evolution of the seasonal amplitude of temperature (red) and precipitation (blue) represented by the projection of these climate variables on the evolution of the seasonal amplitude of insolation as a function of latitude. The solid line stands for the raw signal and the dotted line for the signal after a 100 year smoothing.

Figure 8: a) total change in snow cover ($kg\ m^{-2}$) and sea ice fraction (%) integrated over the last 6000 years, and evolution from the Mid Holocene of annual mean maximum summer and minimum winter values for b) sea ice averages over the northern hemisphere, c) snow (solid lines) and 2-m air temperature (dotted lines) average for all regions north of 60°N, and d) snow and 2m air temperature over Eurasia.in b), c), and d) black, dark blue and light blue stand respectively for the annual mean, maximum and minimum annual monthly values for sea-ice or snow cover, and black, green and red for annual mean, annual minimum and annual maximum air temperature.

Figure 9: Long term evolution of the simulated a) bare soil, b) grass and c) tree covers, expressed as the percentage (%) of Global, NH or SH continental areas, and d) GPP (PgC/y) over the same regions. Annual mean values are smoothed by a 100 year running mean.

Figure 10: Vegetation map comparing a), d), g) the Mid Holocene (first 50 years) and the pre-industrial (50 year around 1850 AC (last 150 to 100 years) periods of the transient simulation , b), d), h) the differences between the historical period (last 50 years) and the pre-industrial period of the transient simulation and c), f), i) the difference between pre-industrial climate for the transient simulation and the PI-Vnone simulations. For simplicity we only consider bare soil (top), grass (middle) and tree (bottom).

Figure 11: Long term evolution of Bare soil, Grass and Tree, expressed as the % of land cover North of 60°N, over Eurasia and over West Africa. The different values are plotted as differences with the first 100 year averages. A 100 year running mean is applied to the curves before plotting.

Figure 12. Evolution of a) the location of the West African monsoon annual mean (black) and maximum (red) rain belt in degrees of latitude and b) annual mean (black), minimum (green) and maximum (red) monthly precipitation ($mm.d^{-1}$) averages over the Sahel region. The first 100 years have been removed and a 100 running mean applied before plotting.

Figure 13: Evolution of the different tree PFTs in Eurasia, expressed as the percentage change compared to their 6000 year BP initial state. Each color line stands for a different PFT. Values have been smoothed by a 100 year running mean.

Figure 14: a) Simulated mega-biome distribution by MH-Vnone, converted from the modelled PFT properties using the default algorithm described in Figure A1. b) and c) Reconstructions in BIOME 6000 DB version 1 for the MH and PI periods (Harrison, 2017). d) Number of pixels where reconstruction is available and the model matches (or does not match) the data. Note that multiple reconstruction sites may be located in the same model grid cell, in which case we did not group them so that each site was counted once. Numbers in parenthesis on the x axis in d) represent the number of sites for each biome type. Same as in c but for the number of matches between e) the BIOME6000 MH (6k) and PI (0k) reconstructions at pollen sites and f) the simulated mega-biomes for MH and PI at each model grid cell.

Figure 15: Impact of the dynamical vegetation and initialization of vegetation on the simulated climate. Differences for annual mean a) c) e) precipitation ($mm.d^{-1}$) and b) d) f) 2m air temperature (°C) between a) and b) the MH in the TRHOLV simulation and the MH simulation without dynamical vegetation (MH FPMIP4), d) and d) the mid Holocene and the pre-industrial simulations in the TTHOLV simulation, and e) and f) the two pre-industrial simulations initialized from bare soil (PI-Vnone) or a vegetation map for vegetation (PI-Vmap). See table 2 and text for details on the simulations.

Figure 16: Difference between Vegetation maps obtained with the two different initial states for a) c) e) mid Holocene simulations, b) d) f) pre-industrial simulations. Vmap stands for MH and PI simulations where the mid-Holocene vegetation has been initialized from a vegetation map and Vnone for MH and PI simulations where the mid-Holocene has been initialized from bare soil. For simplicity we only consider fractions of a) b) bare soil, c) d) grass and e) f) trees.

Figure A1: Parrallel coordinate representation of metrics highlighting model mean bias (left column) and spatial root mean square differences (right column) against observations for the four climatological seasons (Decembre to February, djf; Mars to May, mam; June to August, jja ; September to November, son) for surface air temperature (tas, °C) and precipitation, mmd^{-1}) and Northern Hemisphere extra tropics (NHEX, 20°N-90°N), Tropics (20°S-20°N), and Southern Hemisphere extra tropics (SHEX 90°S-20°S). Each color line stands for a simulations discussed in this manuscript. The results of the different CMIP5 simulations (grey lines) are included for comparison.

Figure A2 : (a) Algorithm to convert the modelled PFT properties into the eight megabiomes provided by BIOME 6000 DB version 1. The default thresholds (in black) are the same as Zhu et al. (2018), while different

values (in red) are tested: GDD_5 (annual growing degree days above 5 ºC) of 500 K days (Joos et al., 2004), FPC (foliage projective cover) of 0.3 and 0.6 (Prentice et al., 2011) Height (average height of all existing tree PFTs) of 10 m (Prentice et al., 2011). (b) Simulated megabiome distribution by MH_Vnone and MH_Vmap, using different conversion methods in (a). (c) The number of pixels where modelled megabiome matches data for each biome type, divided by the total number of available sites for that biome type.

8 References

Abis, B. and Brovkin, V.: Environmental conditions for alternative tree-cover states in high latitudes, Biogeosciences, 14, 511-527, 2017.

Albani, S., Mahowald, N. M., Winckler, G., Anderson, R. F., Bradtmiller, L. I., Delmonte, B., François, R., Goman, M., Heavens, N. G., Hesse, P. P., Hovan, S. A., Kang, S. G., Kohfeld, K. E., Lu, H., Maggi, V., Mason, J. A., Mayewski, P. A., McGee, D., Miao, X., Otto-Bliesner, B. L., Perry, A. T., Pourmand, A., Roberts, H. M., Rosenbloom, N., Stevens, T., and Sun, J.: Twelve thousand years of dust: the Holocene global dust cycle constrained by natural archives, Clim. Past, 11, 869-903, 2015.

Alexandrov, D. V., Bashkirtseva, I. A., and Ryashko, L. B.: Noise-induced transitions and shifts in a climate–vegetation feedback model, Royal Society Open Science, 5, 2018.

Aumont, O. and Bopp, L.: Globalizing results from ocean in situ iron fertilization studies, Global Biogeochemical Cycles, 20, -, 2006.

Bartlein, P. J., Harrison, S. P., Brewer, S., Connor, S., Davis, B. A. S., Gajewski, K., Guiot, J., Harrison-Prentice, T. I., Henderson, A., Peyron, O., Prentice, I. C., Scholze, M., Seppa, H., Shuman, B., Sugita, S., Thompson, R. S., Viau, A. E., Williams, J., and Wu, H.: Pollen-based continental climate reconstructions at 6 and 21 ka: a global synthesis, Climate Dynamics, 37, 775-802, 2011.

Bathiany, S., Claussen, M., and Fraedrich, K.: Implications of climate variability for the detection of multiple equilibria and for rapid transitions in the atmosphere-vegetation system, Climate Dynamics, 38, 1775-1790, 2012.

Berger, A.: Long-term variations of caloric solar radiation resulting from the Earth's orbital elements, Quaternary Research, 9, 139-167, 1978.

Bigelow, N. H., Brubaker, L. B., Edwards, M. E., Harrison, S. P., Prentice, I. C., Anderson, P. M., Andreev, A. A., Bartlein, P. J., Christensen, T. R., Cramer, W., Kaplan, J. O., Lozhkin, A. V., Matveyeva, N. V., Murray, D. F., McGuire, A. D., Razzhivin, V. Y., Ritchie, J. C., Smith, B., Walker, D. A., Gajewski, K., Wolf, V., Holmqvist, B. H., Igarashi, Y., Kremenetskii, K., Paus, A., Pisaric, M. F. J., and Volkova, V. S.: Climate change and Arctic ecosystems: 1. Vegetation changes north of 55 degrees N between the last glacial maximum, mid-Holocene, and present, Journal of Geophysical Research-Atmospheres, 108, 2003.

Boisier, J., Noblet‐Ducoudré, N. d., Pitman, A., Cruz, F., Delire, C., den Hurk, B., Molen, M., Müller, C., and Voldoire, A.: Attributing the impacts of land‐cover changes in temperate regions on surface temperature and heat fluxes to specific causes: Results from the first LUCID set of simulations, Journal of Geophysical Research: Atmospheres, 117, 2012.

Bonfils, C., de Noblet-Ducoure, N., Braconnot, P., and Joussaume, S.: Hot desert albedo and climate change: Mid-Holocene monsoon in North Africa, Journal of Climate, 14, 3724-3737, 2001.

Braconnot, P., Harrison, S. P., Kageyama, M., Bartlein, P. J., Masson-Delmotte, V., Abe-Ouchi, A., Otto-Bliesner, B., and Zhao, Y.: Evaluation of climate models using palaeoclimatic data, Nature Climate Change, 2, 417-424, 2012.

Braconnot, P., Joussaume, S., Marti, O., and de Noblet, N.: Synergistic feedbacks from ocean and vegetation on the African monsoon response to mid-Holocene insolation, Geophys .Res. Lett., 26, 2481-2484, 1999.

Braconnot, P. and Kageyama, M.: Shortwave forcing and feedbacks in Last Glacial Maximum and Mid-Holocene PMIP3 simulations, Phil. Trans. R. Soc. A, 373, 20140424, 2015.

Braconnot, P., Marti, O., and Joussaume, S.: Adjustment and feedbacks in a global coupled ocean-atmosphere model, Climate Dynamics, 13, 507-519, 1997.

Braconnot, P., Otto-Bliesner, B., Harrison, S., Joussaume, S., Peterchmitt, J. Y., Abe-Ouchi, A., Crucifix, M., Driesschaert, E., Fichefet, T., Hewitt, C. D., Kageyama, M., Kitoh, A., Laine, A., Loutre, M. F., Marti, O., Merkel, U., Ramstein, G., Valdes, P., Weber, S. L., Yu, Y., and Zhao, Y.: Results of PMIP2 coupled simulations of the Mid-Holocene and Last Glacial Maximum - Part 1: experiments and large-scale features, Climate of the Past, 3, 261-277, 2007a.

Braconnot, P., Otto-Bliesner, B., Harrison, S., Joussaume, S., Peterchmitt, J. Y., Abe-Ouchi, A., Crucifix, M., Driesschaert, E., Fichefet, T., Hewitt, C. D., Kageyama, M., Kitoh, A., Loutre, M. F., Marti, O., Merkel, U., Ramstein, G., Valdes, P., Weber, L., Yu, Y., and Zhao, Y.: Results of PMIP2 coupled simulations of the Mid-Holocene and Last Glacial Maximum - Part 2: feedbacks with emphasis on the location of the ITCZ and mid- and high latitudes heat budget, Climate of the Past, 3, 279-296, 2007b.

Brovkin, V., Bendtsen, J., Claussen, M., Ganopolski, A., Kubatzki, C., Petoukhov, V., and Andreev, A.: Carbon cycle, vegetation, and climate dynamics in the Holocene: Experiments with the CLIMBER-2 model, Global Biogeochemical Cycles, 16, 2002.

Campbell, J. E., Berry, J. A., Seibt, U., Smith, S. J., Montzka, S. A., Launois, T., Belviso, S., Bopp, L., and Laine, M.: Large historical growth in global terrestrial gross primary production, Nature, 544, 84, 2017.

Claussen, M.: Late Quaternary vegetation-climate feedbacks, Climate of the Past, 5, 203-216, 2009.

Claussen, M. and Gayler, V.: The greening of the Sahara during the mid-Holocene: results of an interactive atmosphere-biome model, Global Ecology and Biogeography Letters, 6, 369-377, 1997.

COHMAP-Members: Climatic changes of the last 18,000 years: observations and model simulations, Science, 241, 1043-1052, 1988.

Crucifix, M., Loutre, M. F., Tulkens, P., Fichefet, T., and Berger, A.: Climate evolution during the Holocene: a study with an Earth system model of intermediate complexity, Climate Dynamics, 19, 43-60, 2002.

d'Orgeval, T., Polcher, J., and de Rosnay, P.: Sensitivity of the West African hydrological cycle in ORCHIDEE to infiltration processes, Hydrol. Earth Syst. Sci., 12, 1387-1401, 2008.

Dallmeyer, A., Claussen, M., and Brovkin, V.: Harmonising plant functional type distributions for evaluating Earth system models, Clim. Past, 15, 335-366, 2019.

Dallmeyer, A., Claussen, M., and Otto, J.: Contribution of oceanic and vegetation feedbacks to Holocene climate change in monsoonal Asia, Clim. Past, 6, 195-218, 2010.

Davis, B. A. S., Brewer, S., Stevenson, A. C., and Guiot, J.: The temperature of Europe during the Holocene reconstructed from pollen data, Quaternary Science Reviews, 22, 1701-1716, 2003.

de Noblet-Ducoudre, N., Claussen, R., and Prentice, C.: Mid-Holocene greening of the Sahara: first results of the GAIM 6000 year BP Experiment with two asynchronously coupled atmosphere/biome models, Climate Dynamics, 16, 643-659, 2000.

de Noblet, N., Prentice, I. C., Joussaume, S., Texier, D., Botta, A., and Haxeltine, A.: Possible role of atmosphere-biosphere interactions in triggering the last glaciation, Geophys. Res. Letters, 23, 3191-3194, 1996.

de Rosnay, P., Polcher, J., Bruen, M., and Laval, K.: Impact of a physically based soil water flow and soil-plant interaction representation for modeling large-scale land surface processes, Journal of Geophysical Research-Atmospheres, 107, 2002.

deMenocal, P., Ortiz, J., Guilderson, T., Adkins, J., Sarnthein, M., Baker, L., and Yarusinsky, M.: Abrupt onset and termination of the African Humid Period: rapid climate responses to gradual insolation forcing, Quaternary Science Reviews, 19, 347-361, 2000.

Ducoudré, N., Laval, K., and Perrier, A.: SECHIBA, a new set of parameterizations of the hydrologic exchanges at the land/atmosphere interface within the LMD atmospheric general circulation model, Journal of Climate, 6, 1993.

Dufresne, J. L., Foujols, M. A., Denvil, S., Caubel, A., Marti, O., Aumont, O., Balkanski, Y., Bekki, S., Bellenger, H., Benshila, R., Bony, S., Bopp, L., Braconnot, P., Brockmann, P., Cadule, P., Cheruy, F., Codron, F., Cozic, A., Cugnet, D., de Noblet, N., Duvel, J. P., Ethe, C., Fairhead, L., Fichefet, T., Flavoni, S., Friedlingstein, P., Grandpeix, J. Y., Guez, L., Guilyardi, E., Hauglustaine, D., Hourdin, F., Idelkadi, A., Ghattas, J., Joussaume, S., Kageyama, M., Krinner, G., Labetoulle, S., Lahellec, A., Lefebvre, M. P., Lefevre, F., Levy, C., Li, Z. X., Lloyd, J., Lott, F., Madec, G., Mancip, M., Marchand, M., Masson, S., Meurdesoif, Y., Mignot, J., Musat, I., Parouty, S., Polcher, J., Rio, C., Schulz, M., Swingedouw, D., Szopa, S., Talandier, C., Terray, P., Viovy, N., and Vuichard, N.: Climate change

projections using the IPSL-CM5 Earth System Model: from CMIP3 to CMIP5, Climate Dynamics, 40, 2123-2165, 2013.
Egerer, S., Claussen, M., Reick, C., and Stanelle, T.: Could gradual changes in Holocene Saharan landscape have caused the observed abrupt shift in North Atlantic dust deposition?, Earth and Planetary Science Letters, 473, 104-112, 2017.
Fichefet, T. and Maqueda, M. A. M.: Modelling the influence of snow accumulation and snow-ice formation on the seasonal cycle of the Antarctic sea-ice cover, Climate Dynamics, 15, 251-268, 1999.
Gleckler, P., Doutriaux, C., Durack, P., Taylor, K., Zhang, Y., Williams, D., Mason, E., and Servonnat, J.: A More Powerful Reality Test for Climate Models, EOS, Transactions of the American Geophysical Union, 97, 2016.
Guimberteau, M., Zhu, D., Maignan, F., Huang, Y., Yue, C., Dantec-Nédélec, S., Ottlé, C., Jornet-Puig, A., Bastos, A., Laurent, P., Goll, D., Bowring, S., Chang, J., Guenet, B., Tifafi, M., Peng, S., Krinner, G., Ducharne, A., Wang, F., Wang, T., Wang, X., Wang, Y., Yin, Z., Lauerwald, R., Joetzjer, E., Qiu, C., Kim, H., and Ciais, P.: ORCHIDEE-MICT (v8.4.1), a land surface model for the high latitudes: model description and validation, Geosci. Model Dev., 11, 121-163, 2018.
Harrison, S.: BIOME 6000 DB classified plotfile version 1, University of Reading. Dataset. , doi: http://dx.doi.org/10.17864/1947.99, 2017. 2017.
Harrison, S. P., Bartlein, P. J., Brewer, S., Prentice, I. C., Boyd, M., Hessler, I., Holmgren, K., Izumi, K., and Willis, K.: Climate model benchmarking with glacial and mid-Holocene climates, Climate Dynamics, 43, 671-688, 2014.
Harrison, S. P., Jolly, D., Laarif, F., Abe-Ouchi, A., Dong, B., Herterich, K., Hewitt, C., Joussaume, S., Kutzbach, J. E., Mitchell, J., de Noblet, N., and Valdes, P.: Intercomparison of Simulated Global Vegetation Distributions in Response to 6 kyr BP Orbital Forcing, Journal of Climate, 11, 2721-2742, 1998.
Held, I. M. and Soden, B. J.: Robust Responses of the Hydrological Cycle to Global Warming, Journal of Climate, 19, 5686-5699, 2006.
Hély, C. and Lézine, A.-M.: Holocene changes in African vegetation: tradeoff between climate and water availability, Climate of the Past, 10, 681-686, 2014.
Hopcroft, P. O., Valdes, P. J., Harper, A. B., and Beerling, D. J.: Multi vegetation model evaluation of the Green Sahara climate regime, Geophysical Research Letters, 44, 6804-6813, 2017.
Hourdin, F., Foujols, M. A., Codron, F., Guemas, V., Dufresne, J. L., Bony, S., Denvil, S., Guez, L., Lott, F., Ghattas, J., Braconnot, P., Marti, O., Meurdesoif, Y., and Bopp, L.: Impact of the LMDZ atmospheric grid configuration on the climate and sensitivity of the IPSL-CM5A coupled model, Climate Dynamics, 40, 2167-2192, 2013.
Jansen, E., Overpeck, J., Briffa, K. R., Duplessy, J. C., Joos, F., Masson-Delmotte, V., Olago, D., Otto-Bliesner, B., Peltier, W. R., Rahmstorf, S., Ramesh, R., Raynaud, D., Rind, D., Solomina, O., Villalba, R., and Zhang, D.: Paleoclimate. In: Climate Chane 2007: The Physical Science Basis. Contribution of Working Group I to the Fourth Assessement Report of the Intergovernmental Panel on Climate Change, Solomon, S., Qin, D. H., Manning, M., Chen, Z., Marsuis, M., Averyt, K. B., Tignor, M., and Miller, H. L. (Eds.), Cambridge University Press, Cambridge, United Kingdom and New York, NY, USA, 2007.
Jolly, D., Prentice, I. C., Bonnefille, R., Ballouche, A., Bengo, M., Brenac, P., Buchet, G., Burney, D., Cazet, J.-P., Cheddadi, R., Edohr, T., Elenga, H., Elmoutaki, S., Guiot, J., Laarif, F., Lamb, H., Lezine, A.-M., Maley, J., Mbenza, M., Peyron, O., Reille, M., Reynaud-Ferrera, I., Riollet, G., Ritchie, J. C., Roche, E., Scott, L., Ssemmanda, I., Straka, H., Umer, M., Van Campo, E., Vilimumbala, S., Vincens, A., and Waller, M.: Biome reconstruction from pollen and plant macrofossil data for Africa and the Arabian peninsula at 0 and 6 ka., Journal of Biogeography, 25, 1007-1028, 1998.
Jomelli, V., Khodri, M., Favier, V., Brunstein, D., Ledru, M. P., Wagnon, P., Blard, P. H., Sicart, J. E., Braucher, R., Grancher, D., Bourles, D. L., Braconnot, P., and Vuille, M.: Irregular tropical glacier retreat over the Holocene epoch driven by progressive warming, Nature, 474, 196-199, 2011.

957 Joos, F., Gerber, S., Prentice, I., Otto-Bliesner, B., and Valdes, P.: Transient simulations of Holocene
958 atmospheric carbon dioxide and terrestrial carbon since the Last Glacial Maximum, GLOBAL
959 BIOGEOCHEMICAL CYCLES, 18, -, 2004.
960 Joos, F. and Spahni, R.: Rates of change in natural and anthropogenic radiative forcing over the past
961 20,000 years, Proceedings of the National Academy of Sciences, 105, 1425-1430, 2008.
962 Joussaume, S. and Braconnot, P.: Sensitivity of paleoclimate simulation results to season definitions,
963 J. Geophys. Res., 102, 1943-1956, 1997.
964 Joussaume, S., Taylor, K. E., Braconnot, P., Mitchell, J. F. B., Kutzbach, J. E., Harrison, S. P., Prentice, I.
965 C., Broccoli, A. J., Abe-Ouchi, A., Bartlein, P. J., Bonfils, C., Dong, B., Guiot, J., Herterich, K., Hewitt, C.
966 D., Jolly, D., Kim, J. W., Kislov, A., Kitoh, A., Loutre, M. F., Masson, V., McAvaney, B., McFarlane, N.,
967 de Noblet, N., Peltier, W. R., Peterschmitt, J. Y., Pollard, D., Rind, D., Royer, J. F., Schlesinger, M. E.,
968 Syktus, J., Thompson, S., Valdes, P., Vettoretti, G., Webb, R. S., and Wyputta, U.: Monsoon changes
969 for 6000 years ago: Results of 18 simulations from the Paleoclimate Modeling Intercomparison
970 Project (PMIP), Geophysical Research Letters, 26, 859-862, 1999.
971 Kageyama, M., Braconnot, P., Bopp, L., Caubel, A., Foujols, M. A., Guilyardi, E., Khodri, M., Lloyd, J.,
972 Lombard, F., Mariotti, V., Marti, O., Roy, T., and Woillez, M. N.: Mid-Holocene and Last Glacial
973 Maximum climate simulations with the IPSL model-part I: comparing IPSL_CM5A to IPSL_CM4,
974 Climate Dynamics, 40, 2447-2468, 2013a.
975 Kageyama, M., Braconnot, P., Bopp, L., Mariotti, V., Roy, T., Woillez, M. N., Caubel, A., Foujols, M. A.,
976 Guilyardi, E., Khodri, M., Lloyd, J., Lombard, F., and Marti, O.: Mid-Holocene and last glacial
977 maximum climate simulations with the IPSL model: part II: model-data comparisons, Climate
978 Dynamics, 40, 2469-2495, 2013b.
979 Kageyama, M., Braconnot, P., Harrison, S. P., Haywood, A. M., Jungclaus, J. H., Otto-Bliesner, B. L.,
980 Peterschmitt, J. Y., Abe-Ouchi, A., Albani, S., Bartlein, P. J., Brierley, C., Crucifix, M., Dolan, A.,
981 Fernandez-Donado, L., Fischer, H., Hopcroft, P. O., Ivanovic, R. F., Lambert, F., Lunt, D. J.,
982 Mahowald, N. M., Peltier, W. R., Phipps, S. J., Roche, D. M., Schmidt, G. A., Tarasov, L., Valdes, P. J.,
983 Zhang, Q., and Zhou, T.: The PMIP4 contribution to CMIP6 – Part 1: Overview and over-arching
984 analysis plan, Geosci. Model Dev., 11, 1033-1057, 2018.
985 Krinner, G., Viovy, N., de Noblet-Ducoudre, N., Ogee, J., Polcher, J., Friedlingstein, P., Ciais, P., Sitch,
986 S., and Prentice, I. C.: A dynamic global vegetation model for studies of the coupled atmosphere-
987 biosphere system, Global Biogeochemical Cycles, 19, -, 2005.
988 Kutzbach, J. E., Bartlein, P. J., Foley, J. A., Harrison, S. P., Hostetler, S. W., Liu, Z., Prentice, I. C., and
989 Webb, T.: Potential role of vegetation feedback in the climate sensitivity of high-latitude regions: A
990 case study at 6000 years BP, Global Biogeochemical Cycles, 10, 727-736, 1996.
991 Lenton, T. M., Held, H., Kriegler, E., Hall, J. W., Lucht, W., Rahmstorf, S., and Schellnhuber, H. J.:
992 Tipping elements in the Earth's climate system, Proceedings of the National Academy of Sciences,
993 105, 1786-1793, 2008.
994 Levis, S., Bonan, G. B., and Bonfils, C.: Soil feedback drives the mid-Holocene North African monsoon
995 northward in fully coupled CCSM2 simulations with a dynamic vegetation model, Climate Dynamics,
996 23, 791-802, 2004.
997 Lezine, A. M., Hely, C., Grenier, C., Braconnot, P., and Krinner, G.: Sahara and Sahel vulnerability to
998 climate changes, lessons from Holocene hydrological data, Quaternary Science Reviews, 30, 3001-
999 3012, 2011.
1000 Lezine, A. M., Ivory, S. J., Braconnot, P., and Marti, O.: Timing of the southward retreat of the ITCZ at
1001 the end of the Holocene Humid Period in Southern Arabia: Data-model comparison, Quaternary
1002 Science Reviews, 164, 68-76, 2017.
1003 Liu, Z., Wang, Y., Gallimore, R., Gasse, F., Johnson, T., deMenocal, P., Adkins, J., Notaro, M., Prenticer,
1004 I. C., Kutzbach, J., Jacob, R., Behling, P., Wang, L., and Ong, E.: Simulating the transient evolution
1005 and abrupt change of Northern Africa atmosphere-ocean-terrestrial ecosystem in the Holocene,
1006 Quaternary Science Reviews, 26, 1818-1837, 2007.
1007 Madec, G.: NEMO ocean engine, 2008.

Marti, O., Braconnot, P., Dufresne, J. L., Bellier, J., Benshila, R., Bony, S., Brockmann, P., Cadule, P., Caubel, A., Codron, F., de Noblet, N., Denvil, S., Fairhead, L., Fichefet, T., Foujols, M. A., Friedlingstein, P., Goosse, H., Grandpeix, J. Y., Guilyardi, E., Hourdin, F., Idelkadi, A., Kageyama, M., Krinner, G., Levy, C., Madec, G., Mignot, J., Musat, I., Swingedouw, D., and Talandier, C.: Key features of the IPSL ocean atmosphere model and its sensitivity to atmospheric resolution, Climate Dynamics, 34, 1-26, 2010.

Mauri, A., Davis, B., Collins, P., and Kaplan, J.: The climate of Europe during the Holocene: a gridded pollen-based reconstruction and its multi-proxy evaluation, Quaternary Science Reviews, 112, 109-127, 2015.

Otto-Bliesner, B., Braconnot, P., Harrison, S., Lunt, D., Abe-Ouchi, A., Albani, S., Bartlein, P., Capron, E., Carlson, A., Dutton, A., Fischer, H., Goelzer, H., Govin, A., Haywood, A., Joos, F., LeGrande, A., Lipscomb, W., Lohmann, G., Mahowald, N., Nehrbass-Ahles, C., Pausata, F., Peterschmitt, J.-Y., Phipps, S., Renssen, H., and Zhang, Q.: The PMIP4 contribution to CMIP6 – Part 2: Two interglacials, scientific objective and experimental design for Holocene and Last Interglacial simulations, Geoscientific Model Development, 10, 3979-4003, 2017.

Otto, J., Raddatz, T., and Claussen, M.: Strength of forest-albedo feedback in mid-Holocene climate simulations, Clim. Past, 7, 1027-1039, 2011.

Otto, J., Raddatz, T., Claussen, M., Brovkin, V., and Gayler, V.: Separation of atmosphere-ocean-vegetation feedbacks and synergies for mid-Holocene climate, Geophysical Research Letters, 36, 2009.

Pausata, F. S., Messori, G., and Zhang, Q.: Impacts of dust reduction on the northward expansion of the African monsoon during the Green Sahara period, Earth and Planetary Science Letters, 434, 298-307, 2016.

Prentice, I. C., Harrison, S. P., and Bartlein, P. J.: Global vegetation and terrestrial carbon cycle changes after the last ice age, New Phytologist, 189, 988-998, 2011.

Prentice, I. C. and Webb, T.: BIOME 6000: reconstructing global mid-Holocene vegetation patterns from palaeoecological records, Journal of Biogeography, 25, 997-1005, 1998.

Renssen, H., Seppä, H., Crosta, X., Goosse, H., and Roche, D. M.: Global characterization of the Holocene Thermal Maximum, Quaternary Science Reviews, 48, 7-19, 2012.

Saint-Lu, M., Braconnot, P., Leloup, J., and Marti, O.: The role of El Niño in the global energy redistribution: a case study in the mid-Holocene, Climate Dynamics, 2016. 1-18, 2016.

Scheffer, M., Hirota, M., Holmgren, M., Van Nes, E. H., and Chapin, F. S.: Thresholds for boreal biome transitions, Proceedings of the National Academy of Sciences, 109, 21384-21389, 2012.

Singarayer, J. S. and Valdes, P. J.: High-latitude climate sensitivity to ice-sheet forcing over the last 120 kyr, Quaternary Science Reviews, 29, 43-55, 2010.

Texier, D., de Noblet, N., Harrison, S. P., Haxeltine, A., Jolly, D., Joussaume, S., Laarif, F., Prentice, I. C., and Tarasov, P.: Quantifying the role of biosphere-atmosphere feedbacks in climate change: coupled model simulations for 6000 years BP and comparison with palaeodata for northern Eurasia and northern Africa, Climate Dynamics, 13, 865-882, 1997.

Torres, O., Braconnot, P., Marti, O., and Gential, L.: Impact of air-sea drag coefficient for latent heat flux on large scale climate in coupled and atmosphere stand-alone simulations, Climate Dynamics, 2018. 1-20, 2018.

Valcke, S.: OASIS3 user's guide (prism-2-5). CERFACS, Toulouse, France, 2006.

Vial, J., Dufresne, J. L., and Bony, S.: On the interpretation of inter-model spread in CMIP5 climate sensitivity estimates, Climate Dynamics, 41, 3339-3362, 2013.

Wang, T., Ottlé, C., Boone, A., Ciais, P., Brun, E., Morin, S., Krinner, G., Piao, S., and Peng, S.: Evaluation of an improved intermediate complexity snow scheme in the ORCHIDEE land surface model, Journal of Geophysical Research: Atmospheres, 118, 6064-6079, 2013.

Wanner, H., Beer, J., Buetikofer, J., Crowley, T. J., Cubasch, U., Flueckiger, J., Goosse, H., Grosjean, M., Joos, F., Kaplan, J. O., Kuettel, M., Mueller, S. A., Prentice, I. C., Solomina, O., Stocker, T. F., Tarasov, P., Wagner, M., and Widmann, M.: Mid- to Late Holocene climate change: an overview, Quaternary Science Reviews, 27, 1791-1828, 2008.

Wohlfahrt, J., Harrison, S. P., and Braconnot, P.: Synergistic feedbacks between ocean and vegetation on mid- and high-latitude climates during the mid-Holocene, Climate Dynamics, 22, 223-238, 2004.
Woillez, M., Kageyama, M., Krinner, G., De Noblet-Ducoudré, N., Viovy, N., and Mancip, M.: Impact of CO2 and climate on the Last Glacial Maximum vegetation: results from the ORCHIDEE/IPSL models, Climate of the Past, 7, 557-577, 2011.
Zhu, D., Ciais, P., Chang, J., Krinner, G., Peng, S., Viovy, N., Peñuelas, J., and Zimov, S.: The large mean body size of mammalian herbivores explains the productivity paradox during the Last Glacial Maximum, Nature Ecology & Evolution, 2, 640-649, 2018.
Zhu, D., Peng, S. S., Ciais, P., Viovy, N., Druel, A., Kageyama, M., Krinner, G., Peylin, P., Ottlé, C., Piao, S. L., Poulter, B., Schepaschenko, D., and Shvidenko, A.: Improving the dynamics of Northern Hemisphere high-latitude vegetation in the ORCHIDEE ecosystem model, Geoscientific Model Development, 8, 2263-2283, 2015.

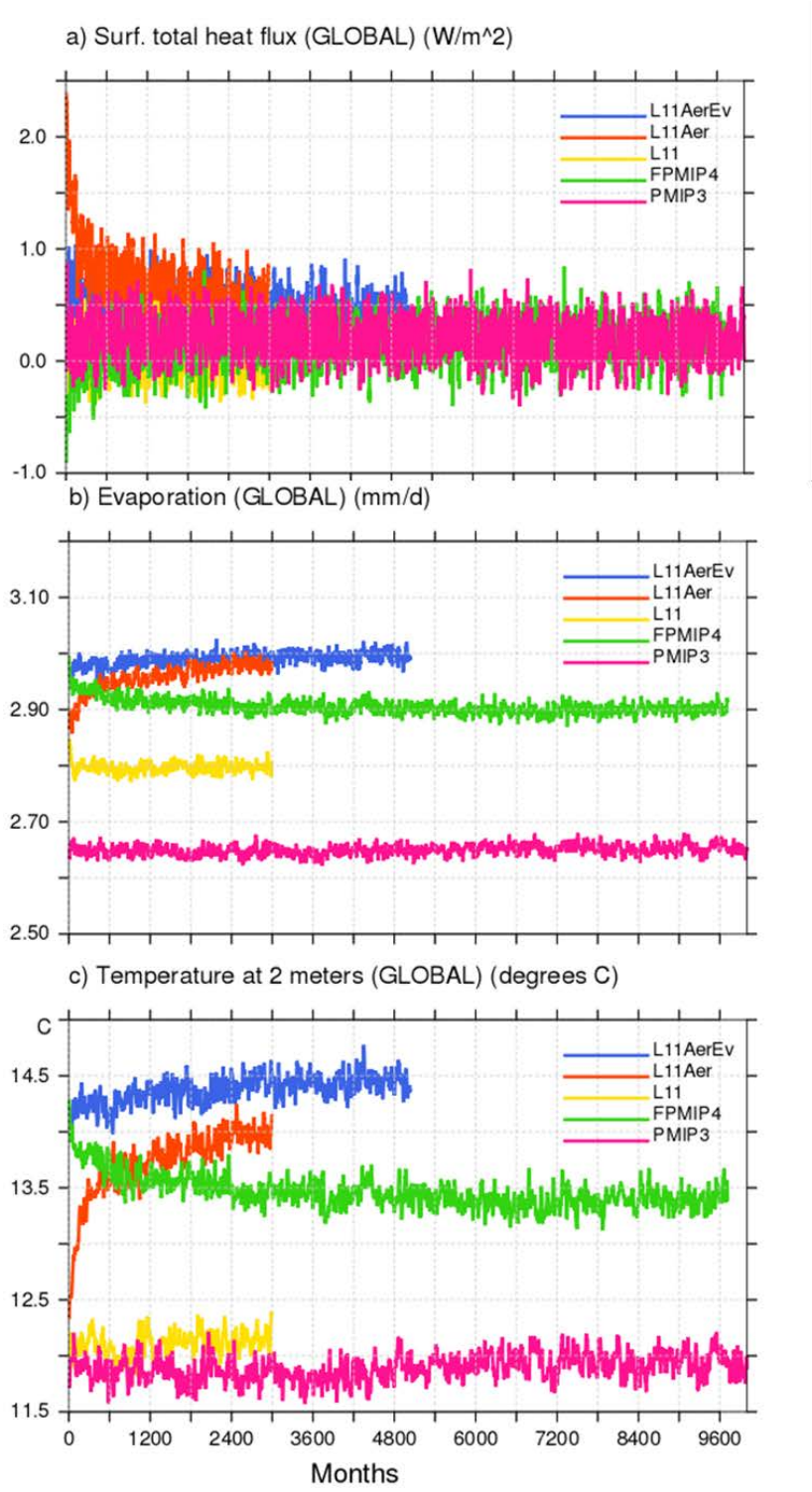

Figure 1: Illustration of the effect of the different adjustments made to produce mid-Holocene simulations with the modified version of the IPSLCM5A-MR version of the IPSL model in which the land surface model ORCHIDEE includes a different soil hydrology and snow models (see text for details). The three panels show the global average of a) net surface heat flux ($W.m^{-2}$), b) evaporation ($kg.m^{-2}$), and c) 2m air temperature (°C). The different color lines represent the results for the different simulations reported in Table 1.

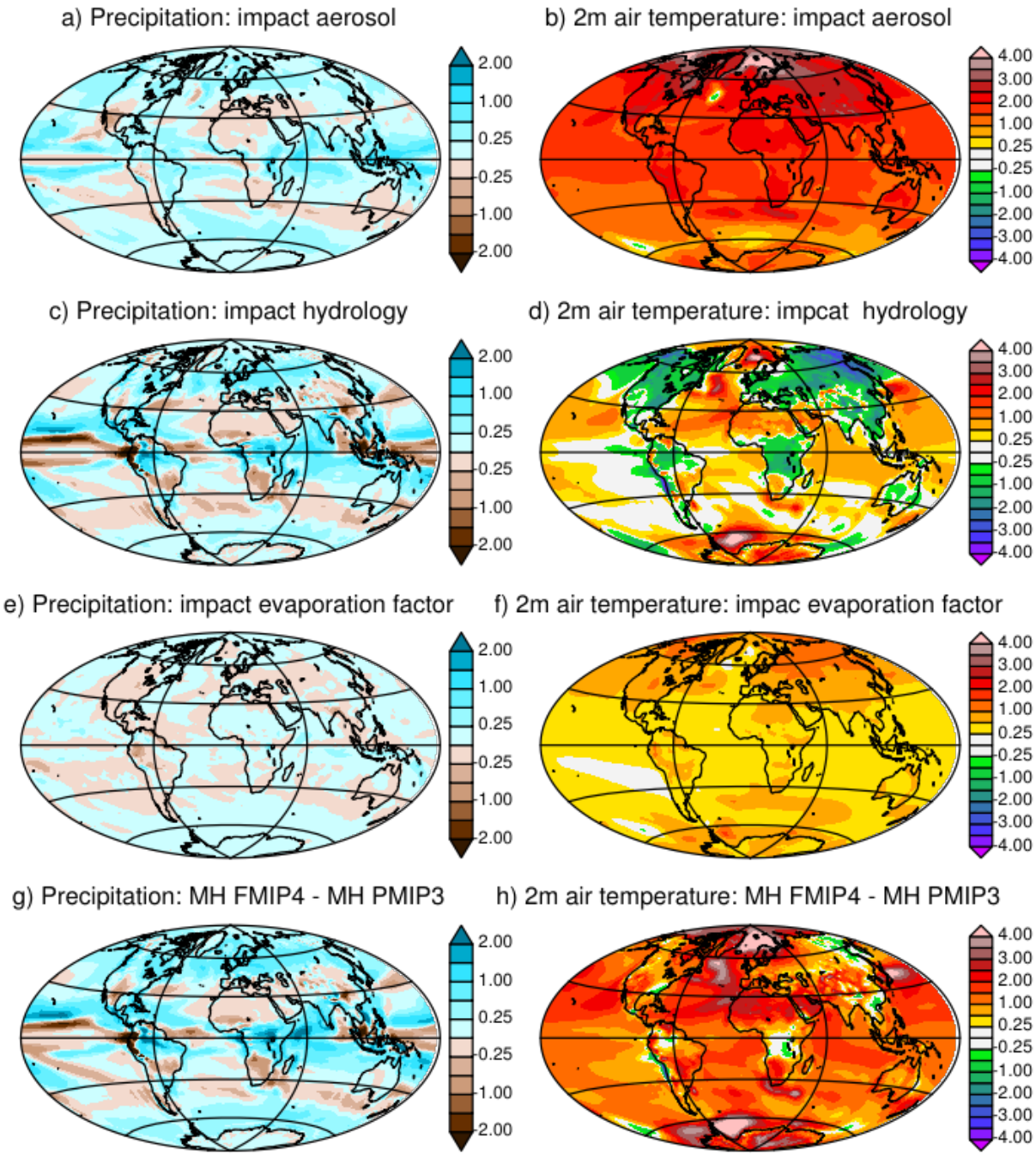

Figure 2: Mid Holocene annual mean precipitation ($mm.d^{-1}$) and 2m air temperature (°C) differences between a) and b) L11Aer and L11, c) and d) L11 and PMIP3, e) and f) PMIP3L11AerEv and L11Aer, and g) and h) FPMIP4 and PMIP3. See Table 1 and text for the details about the different simulations.

.

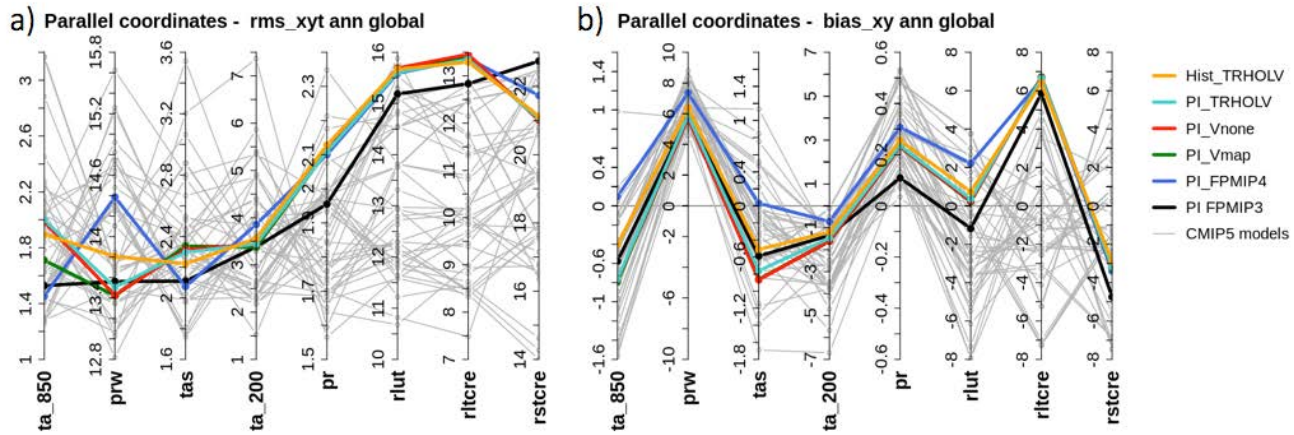

Figure 3. a) Annual mean global model bias (bias_xy) and b) spatio-temporal root mean square differences (rms_xyt) computed on the annual cycle (twelve climatological months) over the globe for the different pre-industrial simulations considered in this manuscript (colors lines) and individual simulations of the CMIP5 multi-model ensemble (grey lines). The metrics for the different variables are presented as parallel coordinates, each of them having their own vertical axis with corresponding values. In these plots, ta stands for temperature (°C) with s for surface, 850 and 200 for 850 and 300 hPa respectively, prw for total water content ($g.kg^{-1}$), pr for precipitation ($mm.d^{-1}$), rlut for outgoing long wave radiation ($W.m^{-2}$), rltcre and rltcre for the cloud radiative effect at the top of the atmosphere in the short wave and long wave radiation respectively ($W.m^{-2}$). See annex A1 for details on the metrics.

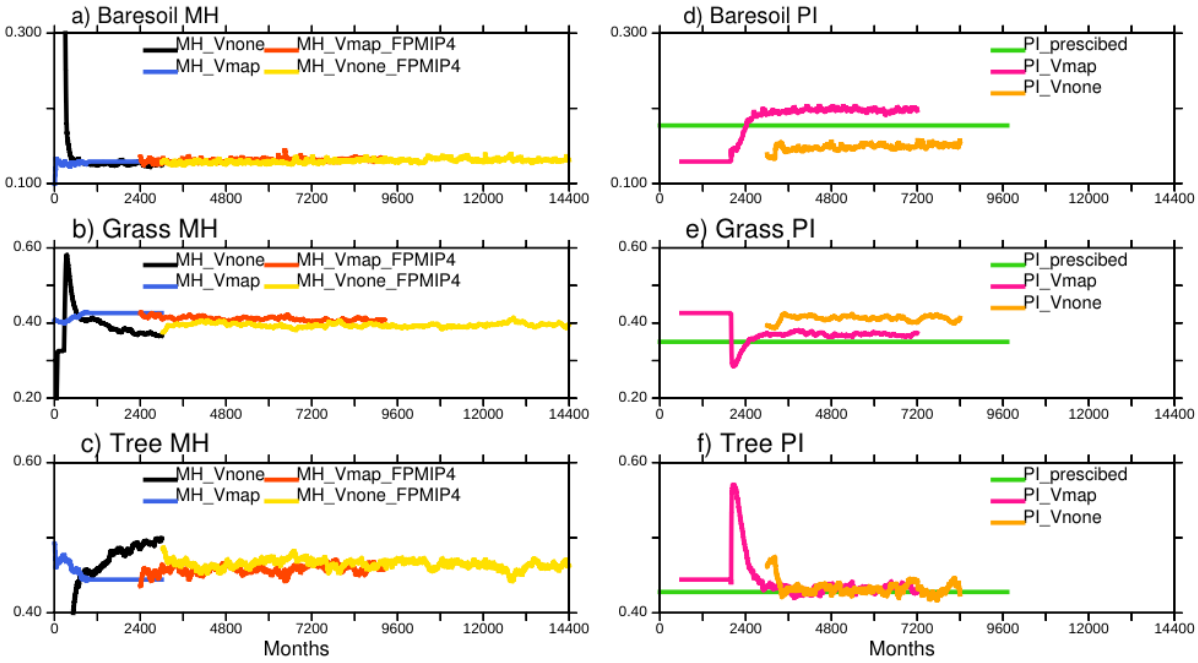

Figure 4. Long term adjustment of vegetation for a), b), and c) mid Holocene (MH) and c), d) and e) preindustrial (PI) climate, when starting from bare soil (Vnone) or from a vegetation map (Vmap). The 13 ORCHIDEE PFTs have been gathered as bare soil, grass, tree and land-use. When the dynamical vegetation is active only natural vegetation is considered. Land-use is thus only present in one simulation, corresponding to a pre-industrial map used as reference in the IPSL model (Dufresne et al. 2013). The corresponding vegetation is referred to as PI_prescribed. The x axis is in months, starting from 0, which allows to plot all the simulation that have their own internal calendar on the same axis.

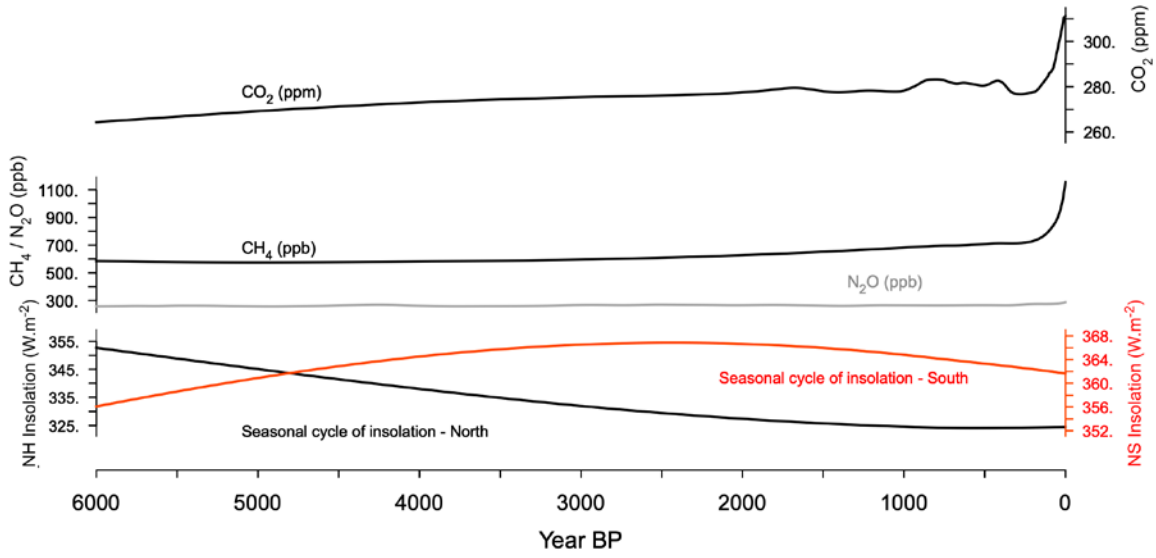

Figure 5: Evolution of trace gases: CO_2 (ppm), CH_4 (ppb) and N_2O (ppb), and seasonal amplitude (maximum annual – minimum annual monthly values) of the incoming solar radiation at the top of the atmosphere ($W.m^{-2}$) averaged over the northern (black line) and the southern (red line) hemispheres. These forcing factors correspond to the PMIP4 experimental design discussed by Otto-Bliesner et al. (2017).

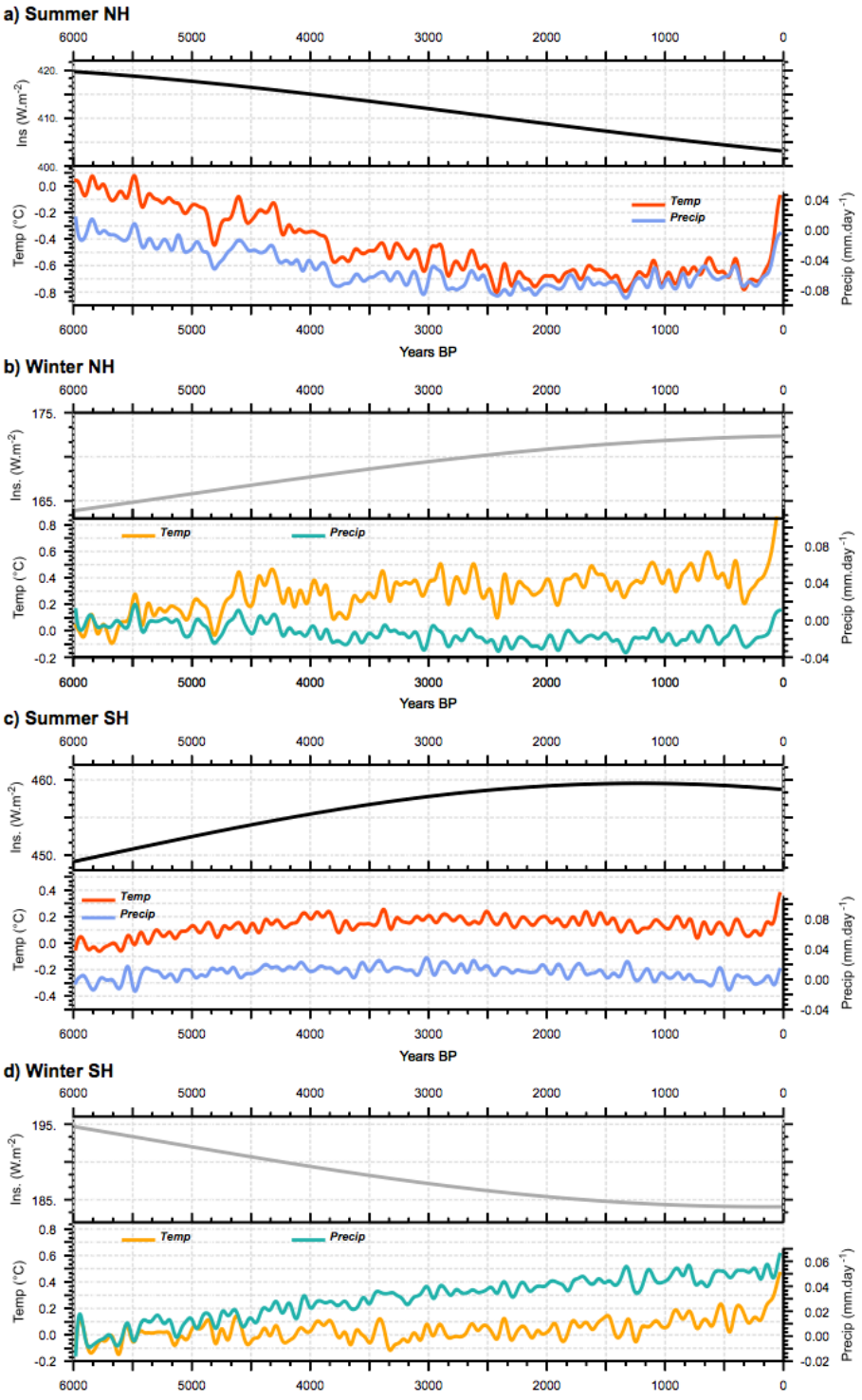

Figure 6. Long term evolution of incoming solar radiation at the top of the atmosphere (TOA)(Wm^{-2}, top panel) and associated response of temperature (°C) and precipitation ($mm.y^{-1}$) expressed as a difference with the 6000 year PB initial state and smoothed by a 100 year running mean) for a) NH Summer, b) NH winter, c) SH summer, and d) SH winter. Temperatures are plotted in red and precipitation in blue for summer, and they are respectively plotted in orange and green for winter. NH Summer and SH Winter correspond to June to September averages whereas NH winter and SH summer correspond to December to March averages. All curves, except insolation, have been smoothed by a 100 year running mean.

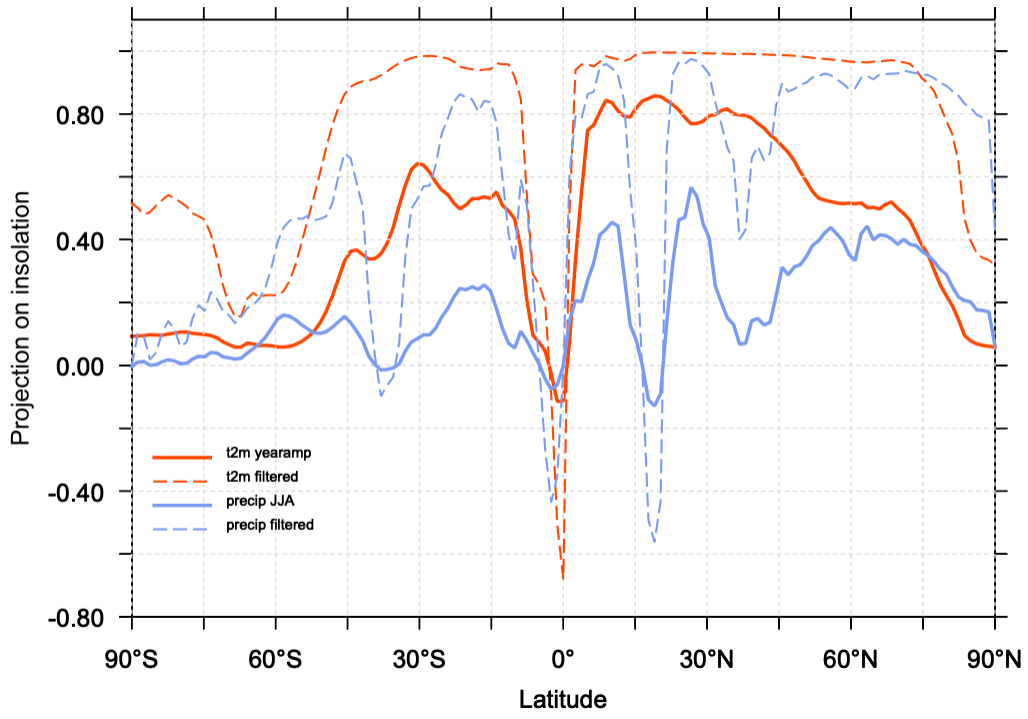

Figure 7: Fraction of the evolution of the seasonal amplitude of temperature (red) and precipitation (blue) represented by the projection of these climate variables on the evolution of the seasonal amplitude of insolation as a function of latitude. The solid line stands for the raw signal and the dotted line for the signal after a 100 year smoothing.

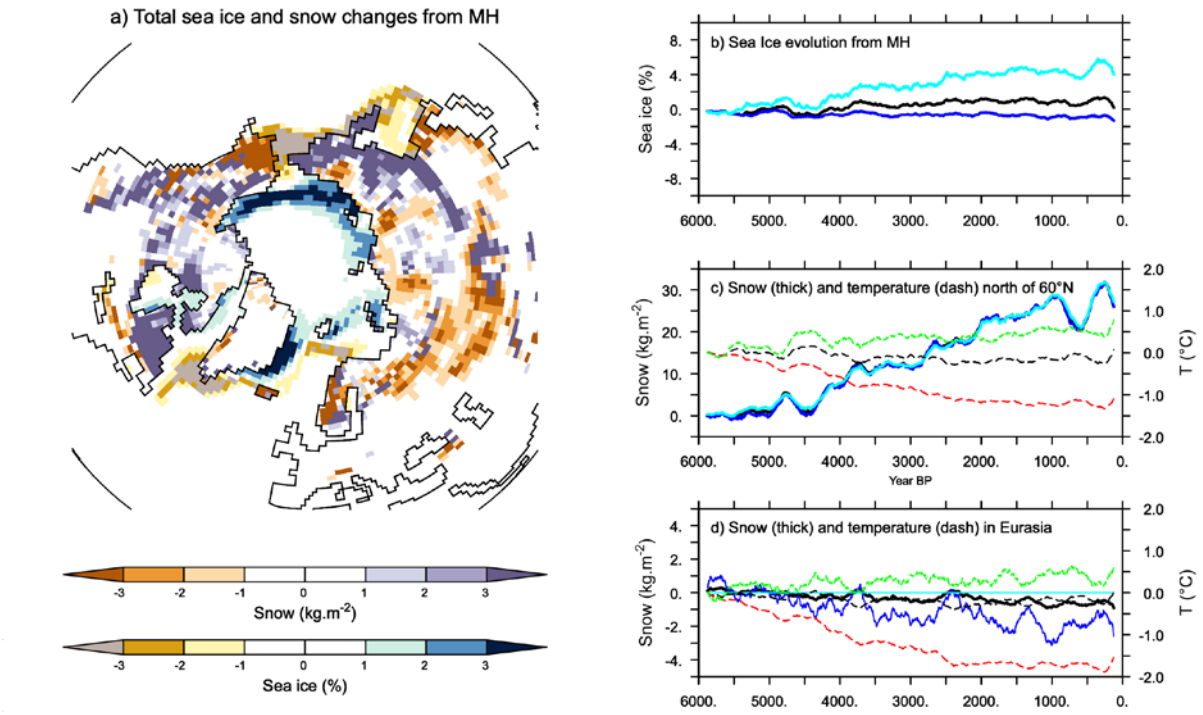

Figure 8: a) total change in snow cover (kg m^{-2}) and sea ice fraction (%) integrated over the last 6000 years, and evolution from the Mid Holocene of annual mean maximum summer and minimum winter values for b) sea ice averages over the northern hemisphere, c) snow (solid lines) and 2-m air temperature (dotted lines) average for all regions north of 60°N, and d) snow and 2m air temperature over Eurasia.in b), c), and d) black, dark blue and light blue stand respectively for the annual mean, maximum and minimum annual monthly values for sea-ice or snow cover, and black, green and red for annual mean, annual minimum and annual maximum air temperature.

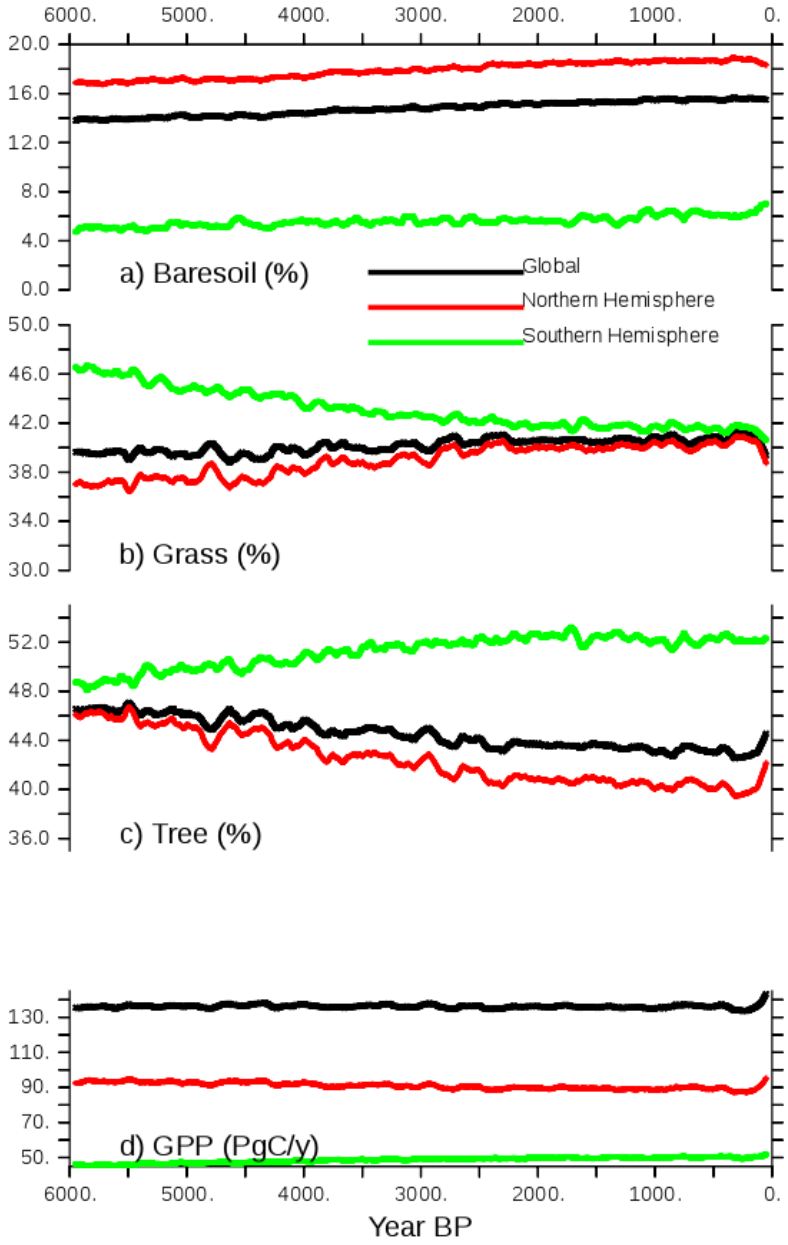

Figure 9: Long term evolution of the simulated a) bare soil, b) grass and c) tree covers, expressed as the percentage (%) of Global, NH or SH continental areas, and d) GPP (PgC/y) over the same regions. Annual mean values are smoothed by a 100 year running mean.

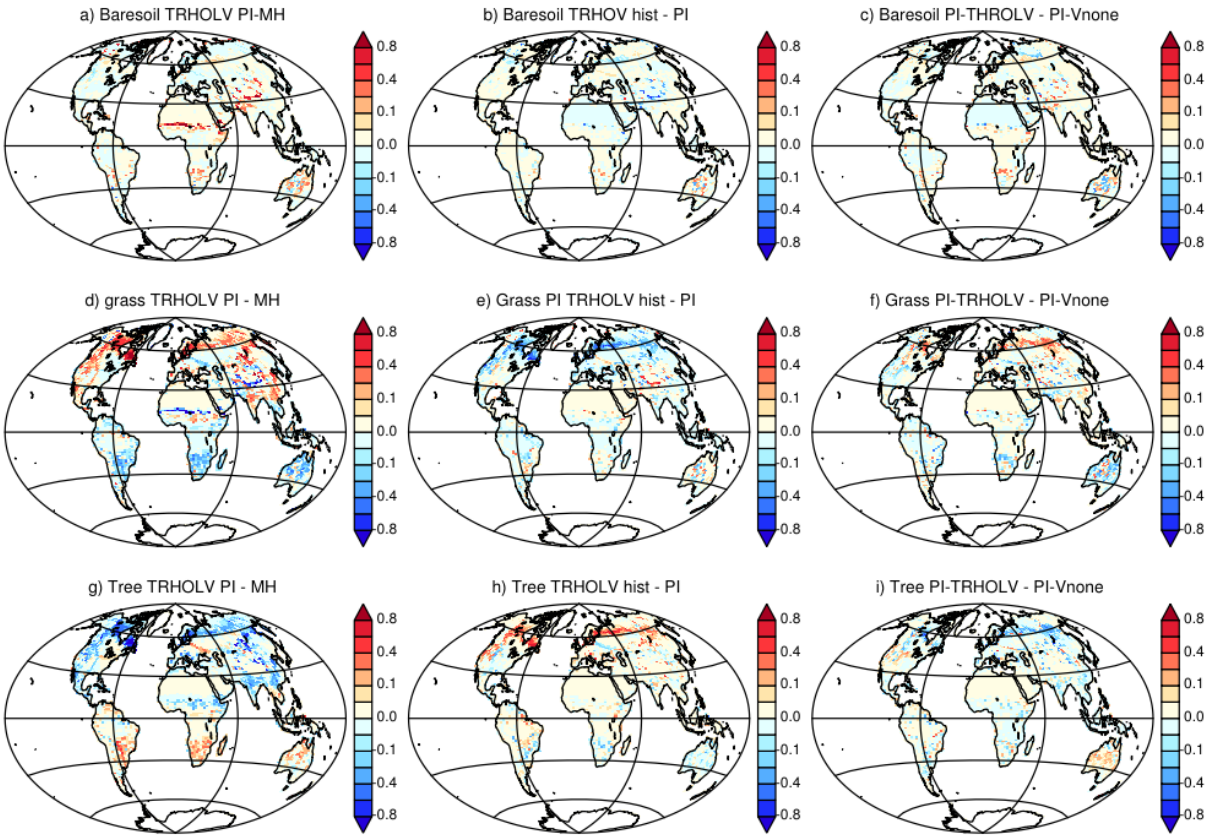

Figure 10: Vegetation map comparing a), d), g) the Mid Holocene (first 50 years) and the pre-industrial (50 year around 1850 AC (last 150 to 100 years) periods of the transient simulation , b), d), h) the differences between the historical period (last 50 years) and the pre-industrial period of the transient simulation and c), f), i) the difference between pre-industrial climate for the transient simulation and the PI-Vnone simulations. For simplicity we only consider bare soil (top), grass

(middle) and tree (bottom).

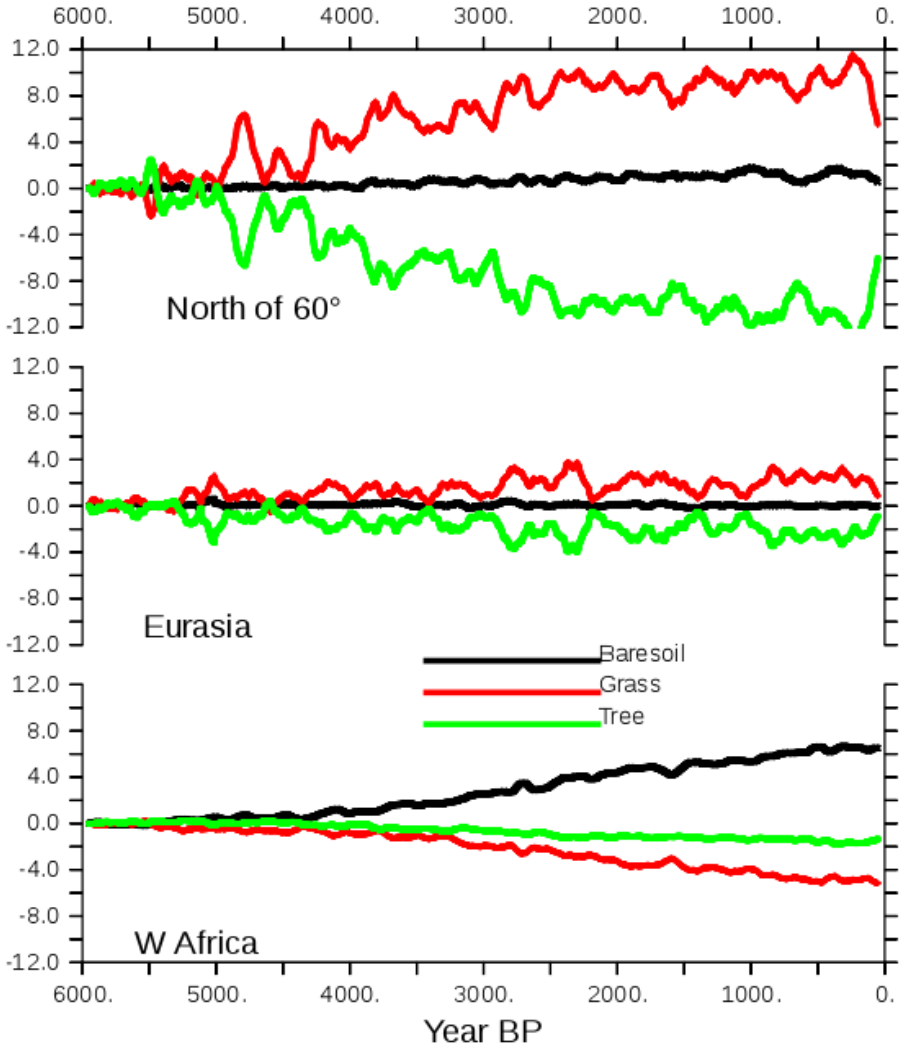

Figure 11: Long term evolution of Bare soil, Grass and Tree, expressed as the % of land cover North of 60°N, over Eurasia and over West Africa. The different values are plotted as differences with the first 100 year averages. A 100 year running mean is applied to the curves before plotting.

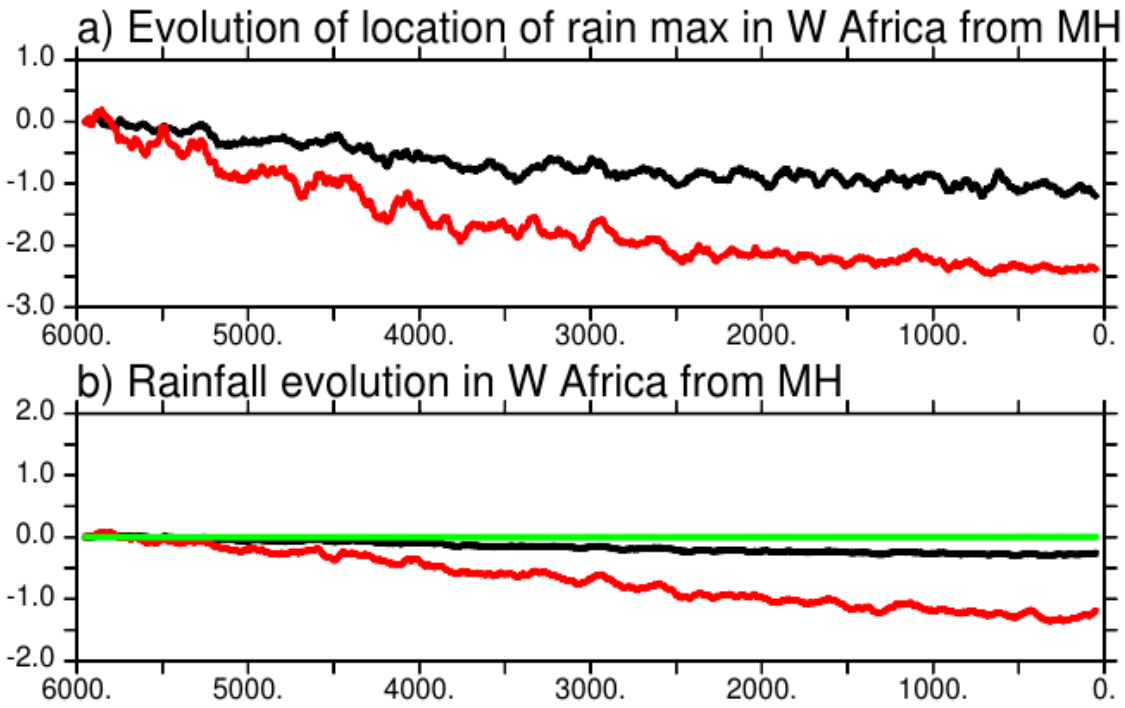

Figure 12. Evolution of a) the location of the West African monsoon annual mean (black) and maximum (red) rain belt in degrees of latitude and b) annual mean (black), minimum (green) and maximum (red) monthly precipitation ($mm.d^{-1}$) averages over the Sahel region. The first 100 years have been removed and a 100 running mean applied before plotting.

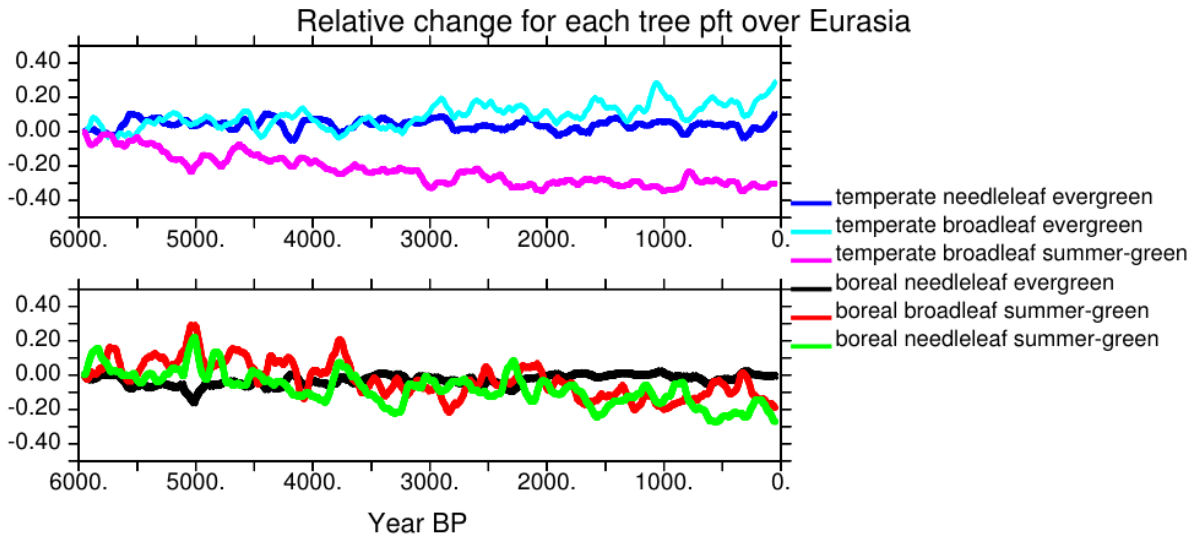

Figure 13: Evolution of the different tree PFTs in Eurasia, expressed as the percentage change compared to their 6000 year BP initial state. Each color line stands for a different PFT. Values have been smoothed by a 100 year running mean.

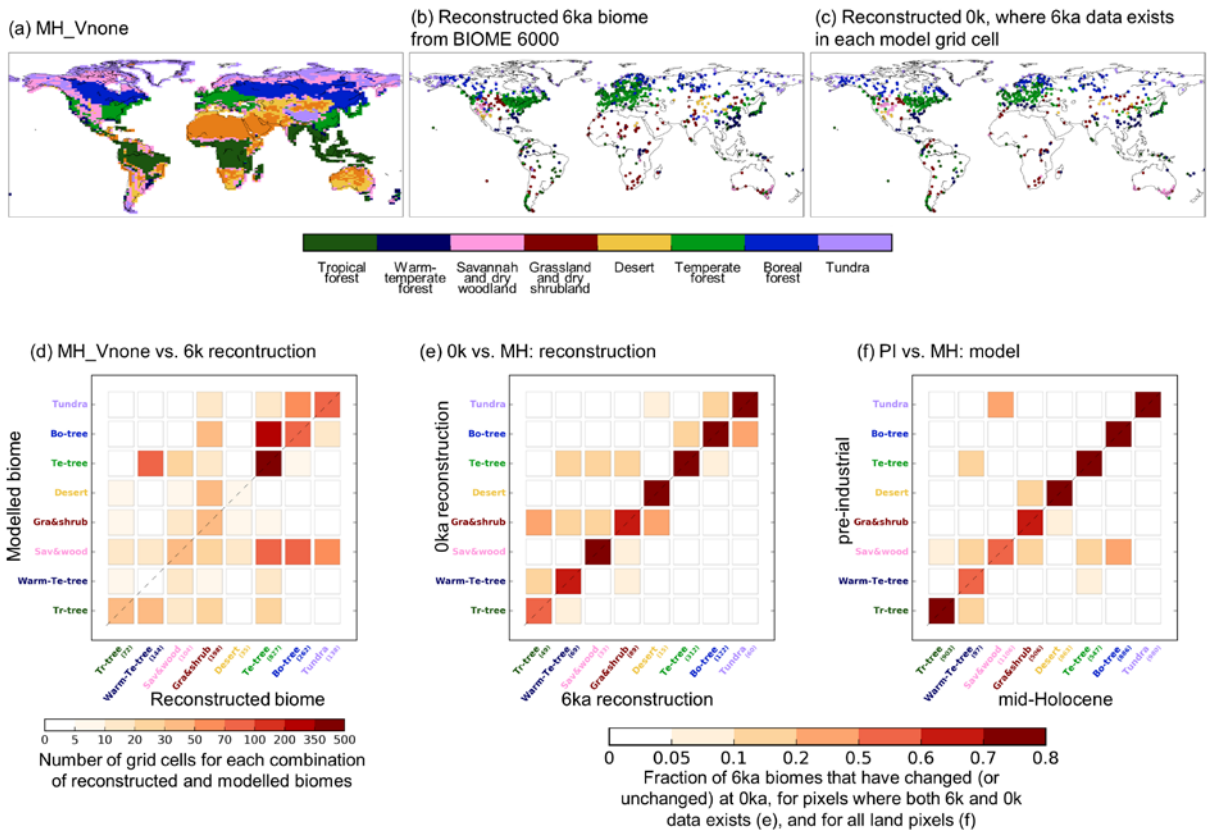

Figure 14: a) Simulated mega-biome distribution by MH-Vnone, converted from the modelled PFT properties using the default algorithm described in Figure A1. b) and c) Reconstructions in BIOME 6000 DB version 1 for the MH and PI periods (Harrison, 2017). d) Number of pixels where reconstruction is available and the model matches (or does not match) the data. Note that multiple reconstruction sites may be located in the same model grid cell, in which case we did not group them so that each site was counted once. Numbers in parenthesis on the x axis in d) represent the number of sites for each biome type. Same as in c but for the number of matches between e) the BIOME6000 MH (6k) and PI (0k) reconstructions at pollen sites and f) the simulated mega-biomes for MH and PI at each model grid cell.

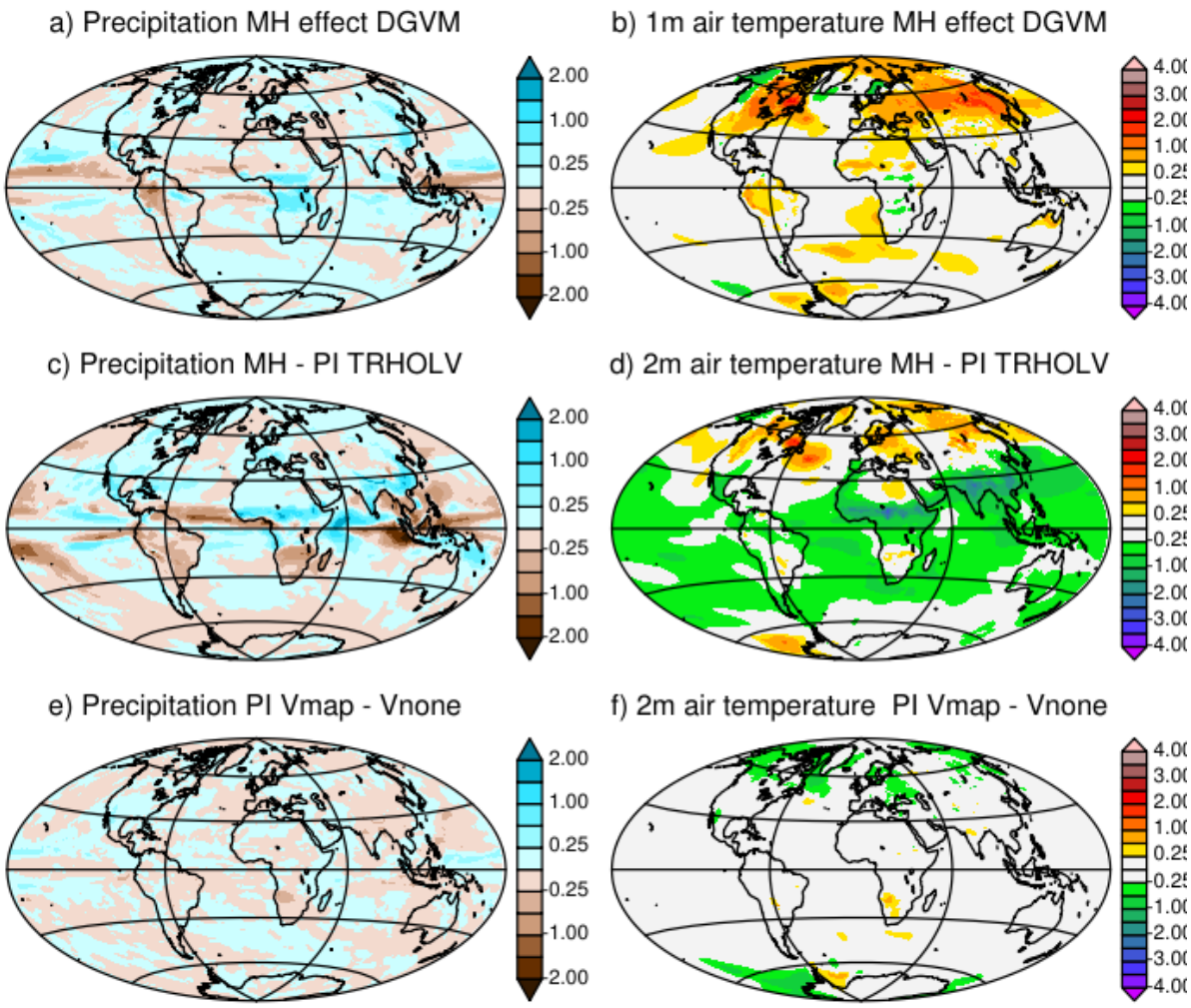

Figure 15: Impact of the dynamical vegetation and initialization of vegetation on the simulated climate. Differences for annual mean a) c) e) precipitation ($mm.d^{-1}$) and b) d) f) 2m air temperature (°C) between a) and b) the MH in the TRHOLV simulation and the MH simulation without dynamical vegetation (MH FPMIP4), d) and d) the mid Holocene and the pre-industrial simulations in the TTHOLV simulation, and e) and f) the two pre-industrial simulations initialized from bare soil (PI-Vnone) or a vegetation map for vegetation (PI-Vmap). See table 2 and text for details on the simulations.

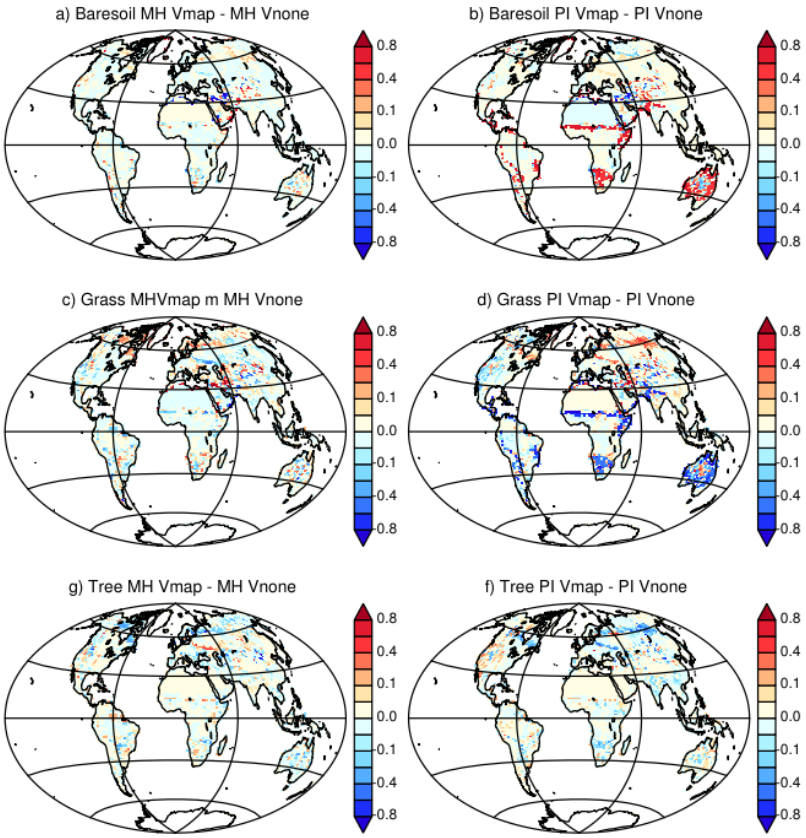

Figure 16: Difference between Vegetation maps obtained with the two different initial states for a) c) e) mid Holocene simulations, b) d) f) pre-industrial simulations. Vmap stands for MH and PI simulations where the mid-Holocene vegetation has been initialized from a vegetation map and Vnone for MH and PI simulations where the mid-Holocene has been initialized from bare soil. For simplicity we only consider fractions of a) b) bare soil, c) d) grass and e) f) trees.

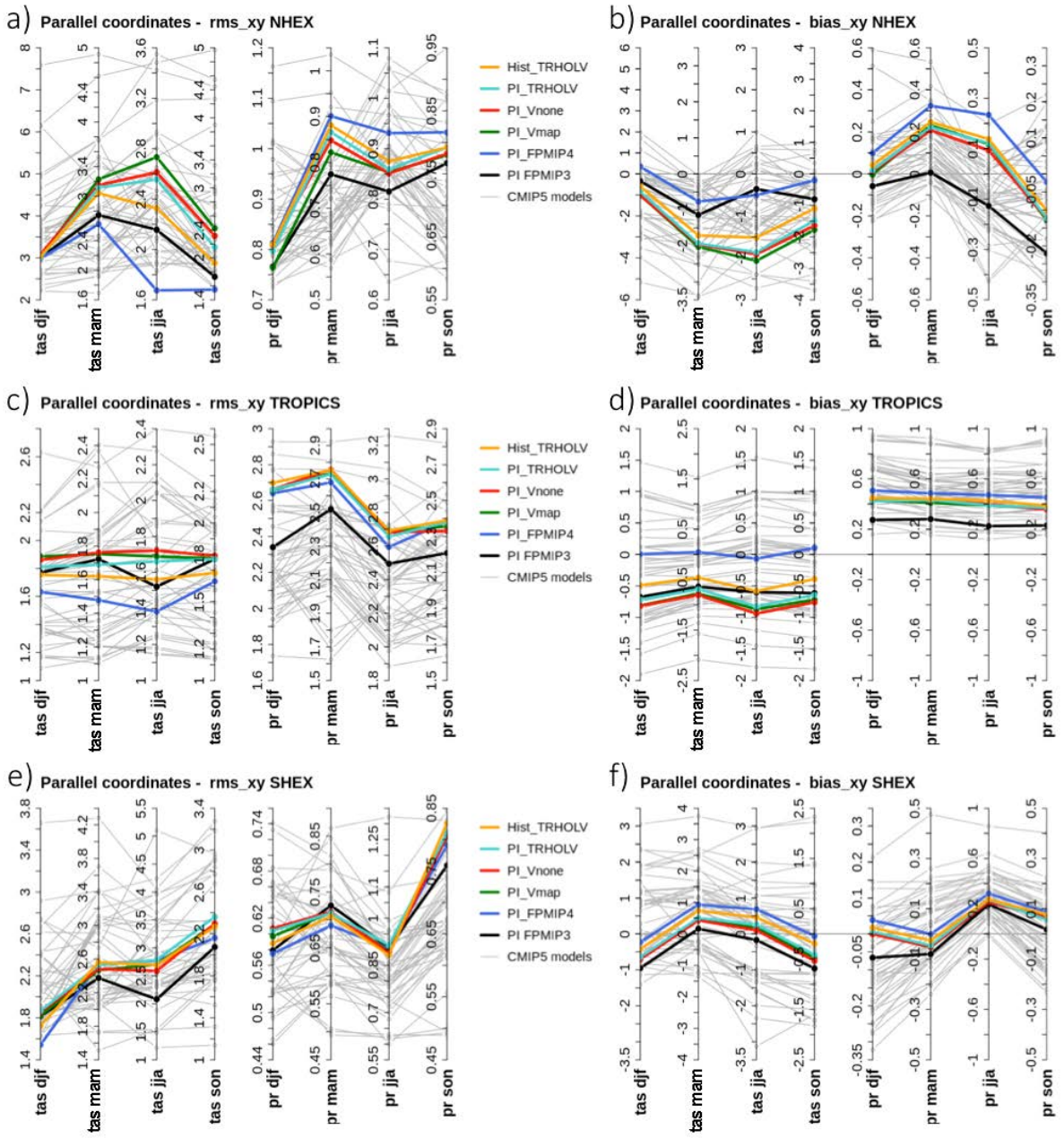

Figure A1: Parrallel coordinate representation of metrics highlighting model mean bias (left column) and spatial root mean square differences (right column) against observations for the four climatological seasons (Decembre to February, djf; Mars to May, mam; June to August, jja ; September to November, son) for surface air temperature (tas, °C) and precipitation, mmd^{-1}) and Northern Hemisphere extra tropics (NHEX, 20°N-90°N), Tropics (20°S-20°N), and Southern Hemisphere extra tropics (SHEX 90°S-20°S). Each color line stands for a simulations discussed in this manuscript. The results of the different CMIP5 simulations (grey lines) are included for comparison.

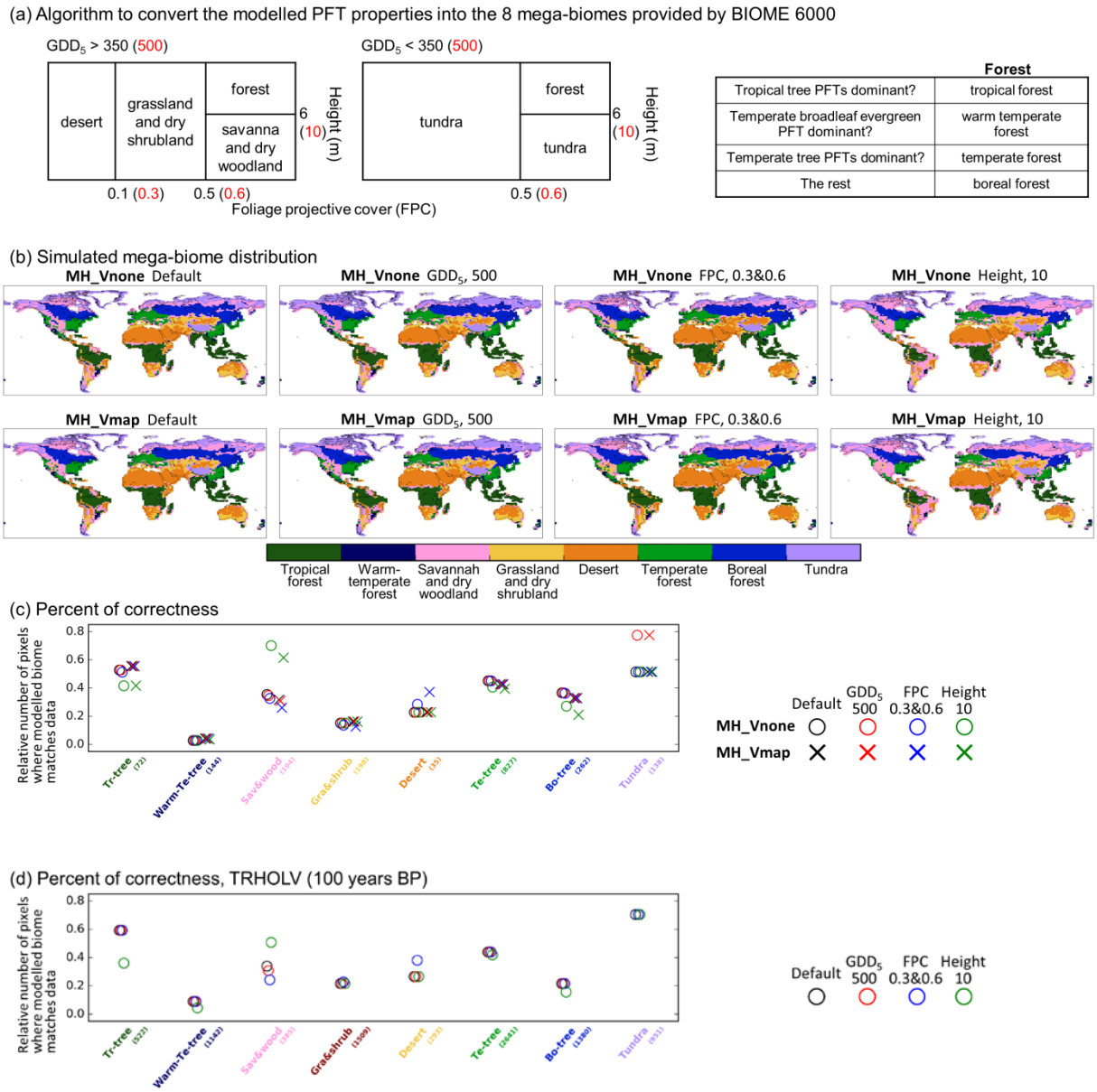

Figure A2 : (a) Algorithm to convert the modelled PFT properties into the eight megabiomes provided by BIOME 6000 DB version 1. The default thresholds (in black) are the same as Zhu et al. (2018), while different values (in red) are tested: GDD_5 (annual growing degree days above 5 ºC) of 500 K days (Joos et al., 2004), FPC (foliage projective cover) of 0.3 and 0.6 (Prentice et al., 2011) Height (average height of all existing tree PFTs) of 10 m (Prentice et al., 2011). (b) Simulated megabiome distribution by MH_Vnone and MH_Vmap, using different conversion methods in (a). (c) The number of pixels where modelled megabiome matches data for each biome type, divided by the total number of available sites for that biome type.